

# From biting to engulfment: curvature–actin coupling controls phagocytosis of soft, deformable targets

Shubhadeep Sadhukhan,<sup>1,\*</sup> Caitlin E. Cornell,<sup>2</sup> Mansehaj Kaur Sandhu,<sup>3</sup> Youri Peeters,<sup>4</sup> Samo Penič,<sup>5</sup> Aleš Iglič,<sup>5</sup> Daniel A. Fletcher,<sup>2,6,7,8</sup> Valentin Jaumouillé,<sup>3</sup> Daan Vorselen,<sup>4</sup> and Nir S. Gov<sup>1,9,†</sup>

<sup>1</sup>*Department of Chemical and Biological Physics, Weizmann Institute of Science, Rehovot, Israel*

<sup>2</sup>*Department of Bioengineering, University of California Berkeley; Berkeley, CA USA*

<sup>3</sup>*Department of Molecular Biology and Biochemistry, Simon Fraser University, Burnaby BC, Canada*

<sup>4</sup>*Department of Cell Biology and Immunology, Wageningen University and Research, Wageningen, the Netherlands*

<sup>5</sup>*Laboratory of Physics, Faculty of Electrical Engineering, University of Ljubljana, Ljubljana, Slovenia*

<sup>6</sup>*University of California Berkeley/University of California San Francisco Graduate Group in Bioengineering, CA USA*

<sup>7</sup>*Division of Biological Systems and Engineering,  
Lawrence Berkeley National Laboratory; Berkeley CA USA*

<sup>8</sup>*Chan Zuckerberg Biohub; San Francisco CA USA*

<sup>9</sup>*Department of Physiology, Development and Neuroscience,  
Downing Site, University of Cambridge, Cambridge, UK*

(Dated: January 29, 2026)

Phagocytosis is a fundamental process of the innate immune system, yet the physical determinants that govern the engulfment of soft, deformable targets remain poorly understood. Existing theoretical models typically approximate targets as rigid particles, overlooking the fact that both immune cells and many biological targets undergo significant membrane deformation during contact. Here, we develop a Monte Carlo-based membrane simulation framework to model the interactions of multiple vesicles, enabling us to explore phagocytosis-like processes in systems where both the phagocyte and the target possess flexible, thermally fluctuating membranes. We first validate our approach against established observations for the engulfment of rigid objects. We then investigate how the mechanical properties of a soft target—specifically membrane bending rigidity govern the outcome of phagocytic interactions. Our simulations reveal three distinct mechanical regimes: (i) biting or trogocytosis, in which the phagocyte extracts a portion of the target vesicle; (ii) pushing, where the target is displaced rather than engulfed; and (iii) full engulfment, in which the target is completely internalized. Increasing membrane tension via internal pressure produces analogous transitions, demonstrating a unified mechanical origin for these behaviours. Qualitative comparison with experiments involving Giant Unilamellar Vesicles (GUVs, deformable microparticles) and lymphoma cells supports the relevance of these regimes to biological phagocytosis. Together, these results highlight how target deformability fundamentally shapes phagocytic success and suggest that immune cells may exploit mechanical cues to recognize among different classes of soft targets.

**Significance statement**—Phagocytosis is essential for immune defence, yet the physical principles governing the engulfment of soft, deformable targets remain poorly understood. Most theoretical models assume rigid particles, even though real cells undergo substantial shape changes during contact. Here, we develop a theoretical membrane model to simulate interactions between multiple vesicles, enabling a mechanistic exploration of phagocytosis of soft targets. We show that target membrane rigidity dictates whether it is fully engulfed, pushed away, or partially bitten. These mechanically driven regimes explain experimental observations of immune cells engaging with both artificial GUVs and lymphoma cells.

## INTRODUCTION

Fundamental biological processes, such as phagocytosis, involve cells adhering and engulfing external objects

[1, 2]. This process has been extensively explored experimentally, and is known to involve the dynamic recruitment of the actin cytoskeleton which plays a crucial role in driving the growth of the membrane protrusion that wraps around the engulfed object [3–5]. However, how the actin recruitment and the resulting cytoskeletal force is coordinated with the membrane dynamics during this process is not well understood [6, 7].

We have recently shown that the actin coordination during phagocytosis of rigid objects can be explained very well by a theoretical model which includes a coupling between curved membrane protein complexes (CMC) that recruit and nucleate actin polymerization [8]. This model demonstrated that passive CMC can enhance the engulfment process, even in the absence of active forces (which represent the protrusive forces due to actin polymerization). Active protrusive forces that are recruited by the CMC enable even more robust engulfment, at lower adhesion energies and less sensitive to the object’s shape. Curved membrane proteins that recruit actin polymerization have been found experimentally to be associated with the leading edge of cellular protrusions [9, 10], which are involved in cellular adhesion, spread-

\* shubhadeep.sadhukhan@weizmann.ac.il

† nir.gov@weizmann.ac.il

ing and motility [11–13]. The theoretical model demonstrated that this curvature-actin activity coupling can explain many cellular shape and migration dynamics [14–16].

Motivated by these results, we explore here the interactions between a cell and a non-rigid object. We extend our model to allow for two vesicle-like surfaces to evolve and interact. The model predicts a spontaneous symmetry breaking between two symmetric vesicles containing passive CMC. For active CMC interacting with a soft passive vesicle, the model predicts different dynamic regimes which depend on the rigidity of the target: with increasing rigidity the active vesicle transitions from “biting”, to “pushing” and eventually “engulfing” the target. These transitions arise in this model purely from the physical interactions, and the curvature-force coupling. These theoretical results offer an explanation of recent experimental observations of immune cells interacting with artificial particles [17–19], vesicles [20] and cancer cells [21] of different rigidities, where both engulfment (phagocytosis) and biting (trophocytosis [22]) were observed.

## THEORETICAL MODEL

Our theoretical model is based on the Monte-Carlo (MC) calculation of the dynamics of a closed three-dimensional triangulated self-avoiding vesicle with a spherical topology (Fig.1) [14, 23, 24] (See SI sections S1-S3 and Method and material for details). Within this model we denote the bare membrane nodes in blue, and the nodes containing the CMC in red. The active protrusive forces, representing the result of actin polymerization, are applied at the locations of the CMC. Our model is purely a membrane model, and it does not include any information about the details of the actin network inside the vesicle or the internal structure of the cell, such as organelles (nucleus) or bulk elastic deformations and their associated energy cost.

Here we developed our previous model to allow for the interaction between two dynamic vesicles (Fig.1). As a first step, we find the nodes that are adjacent between the two vesicles (Fig.1A). Such proximal nodes are restricted in their MC moves, as we do not allow the two vesicles to pass through each other. We need to check any such pair of vertices from different vesicles (Fig.1B, Fig.S1).

Next, we consider the active forces that a vesicle exerts on its neighboring vesicle. Any vertex in vesicle 1 feels the active force due to the other vesicle’s active CMC sites, that are within the interaction range (Fig.1C). The effect of this active force is included by adding the energy term given by,

$$W_{\text{int}} = F \sum_i \hat{n}_i \cdot \vec{dr} \quad (1)$$

where  $i$  runs through all the vertices belonging to vesicle 2 within the distance of  $l_{\min}$  from the vertex of interest

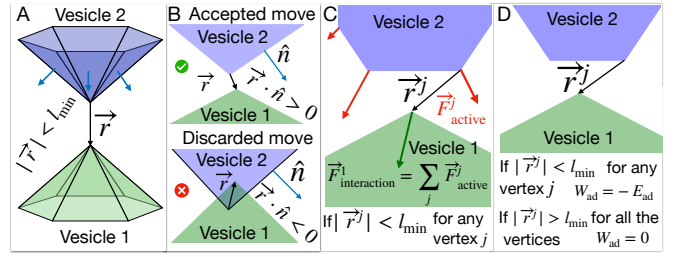


FIG. 1. Interaction between two vesicles in the model: A) Two surfaces of two vesicles are shown in green and blue colors respectively. We check the distance between the vertices that belong to the two different vesicles and determine if they are interacting if the distance between them is less than the length unit of our simulation, i.e.,  $l_{\min}$ . B) If the distance  $|\vec{r}|$  is less than  $l_{\min}$ , we find the dot product between the vector  $\vec{r}$  and the normals of all the triangles common to the vertex from the other vesicle  $\hat{n}$ . If the dot product is negative, the MC move is discarded as the vesicles are overlapping; otherwise, it is accepted. C) The interaction force on the vertex of interest is the vector sum of the active forces applied by the vertices on the other vesicle within the interaction range. D) If a vertex from vesicle 1 is at a distance less than the interaction range  $l_{\min}$  from any vertex of another vesicle, then the adhesive energy between them is  $-E_{\text{ad}}$  for both of these vertices. Otherwise, it is zero.

in vesicle 1, the force vectors have amplitude  $F$  and are directed at the outwards normal  $\hat{n}_i$  at the sites  $i$ , while  $\vec{dr}$  is the MC move of the vertex in vesicle 1. Note that in our model we do not explicitly maintain force balance. When adhered to external surfaces, they serve as momentum sinks, while for free vesicles we work in the center-of-mass frame which allows us to calculate relative shape changes, such that globally the force is effectively balanced.

Finally, we introduce an adhesion energy between proximal vertices on the two neighboring vesicles. Each vertex  $j$  that is within the adhesion range to the other vesicle (Fig.1D) has an adhesion energy that is given by,

$$W_{\text{ad}}^j = -E_{\text{ad}} \quad (2)$$

Initially, we evolve it for a few Monte-Carlo steps from a pentagonal-dipyramid, until it becomes nearly spherical. The active force (when implemented) is set to  $F = 2k_B T / l_{\min}$  and the protein-protein interaction energy is set to  $w = 1k_B T$  throughout the paper.

The area of the vesicles in our model is roughly conserved, with the bond lengths limited in their allowed range of fluctuation ( $l_{\min} < l < 1.7l_{\min}$ ) [23]. The typical changes in area in our simulations (without applied osmotic pressure) are of order 5% (see Fig.S7). When the osmotic pressure is applied inside the vesicle, the bond lengths are pushed towards their maximal allowed value (and therefore the average area increases), and the fluctuations in area are greatly suppressed.

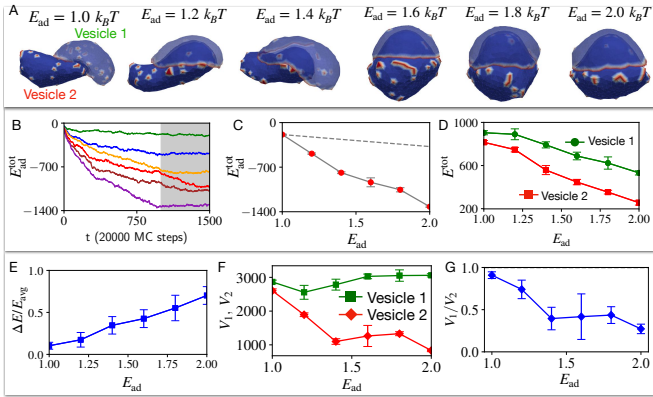


FIG. 2. Two identical vesicles adhere to each other for different strengths of adhesion energy parameter  $E_{\text{ad}}$ . A) Final configuration snapshots of the pair of passive vesicles (at time step  $t = 1500$ ), for the adhesion energy parameter  $E_{\text{ad}} = 1, 1.2, 1.4, 1.6, 1.8, 2.0$  in units of  $k_B T$ . Blue denotes the bare membrane nodes, while red at the passive CMC nodes. B) The average adhesive energy  $E_{\text{ad}}^{\text{tot}}$  per vesicle is shown as a function of timestep for  $E_{\text{ad}} = 1, 1.2, 1.4, 1.6, 1.8, 2.0$  in units of  $k_B T$  with green, blue, orange, red, brown and purple solid lines respectively. C) The final total adhesive energy  $E_{\text{ad}}^{\text{tot}}$  (averaged over the grey shaded time window shown in (B)) is shown for six different values of  $E_{\text{ad}}$ . The grey dashed line represents the total adhesive area in the case of  $E_{\text{ad}} = 1 k_B T$  multiplied by the  $E_{\text{ad}}$ . It shows that the total adhesive energy increases due to the increase in adhered area, faster than the increase in  $E_{\text{ad}}$  (dashed line). In D) we show the total energies the pair of vesicles, averaged over the grey shaded region for six different values of  $E_{\text{ad}}$ . E) The relative difference between the vesicles increases with  $E_{\text{ad}}$ . F) Average volumes of the vesicles as function of  $E_{\text{ad}}$ , and G) the corresponding volume ratio. We used 722 vertices for each vesicle, out of which 50 vertices represent the curved-protein complexes with intrinsic curvature  $c_0 = 1 l_{\text{min}}^{-1}$ , i.e. the CMC percentage is  $\rho = 6.93\%$ . Here, volume is not conserved.

## RESULTS

### Spontaneous symmetry breaking of adhering vesicles containing CMC

We first analyzed the adhesion between two identical vesicles, in the absence of active forces ( $F = 0$ ). For calibration purposes, we tested our model for adhesion of bare membrane vesicles (no CMC) and under the conditions of volume conservation (Figs.S2-S4, See SI section S6), for which analytic solutions are available [25]. In this limit, we could extract the contact angles between the two vesicles, and compare them to an analytic result [26–28]. The agreement between the simulations and the analytic calculation serves to validate our numerical procedure. Adding CMC induces larger spreading and some breaking of the rotational symmetry, though the two adhering vesicles remain symmetric with respect to each other (Fig.S4). In the presence of CMC the contact surface between the vesicles is not anymore composed of

flat or spherical surfaces, as was found for simple adhered vesicles [25, 29].

When we remove the volume conservation constraint (See SI section S7), we find that the presence of CMC can drive a spontaneous symmetry breaking above a critical value of the adhesion energy (Fig.2A). At low adhesion strength the two vesicles are still symmetric (Fig.2A,  $E_{\text{ad}} = 1 k_B T$ ), but above a critical adhesion strength one of the vesicles spontaneously forms a cup-like shape (top vesicle in Fig.2A, vesicle 2), which partially encapsulates the other vesicle (bottom vesicle in Fig.2A, vesicle 1). The CMC in the top vesicle condense along the sharp rim of the cup shape, similar to the organization of such a vesicle when engulfing a rigid sphere [8] (Fig.3A). The bottom vesicle remains largely spherical, with the CMC randomly spread as small isolated clusters. This transition is driven by a lowering of the total energy of the two vesicles. The bending energy increases during the symmetry-breaking transition (Fig.S5), as the cup-shaped vesicle 2 is highly curved. However, this increase is offset by the adhesion energy between the vesicles which decreases the total energy (Fig.2B-E), and to a much smaller amount by the CMC-CMC binding energy (Fig.S5). The huge changes to the volume of the cup-shaped vesicle 2 during this spontaneous shape transition are quantified in Fig.2F,G.

Shapes that are similar to the vesicle pair of Fig.2(A) were obtained for adhering soft tissues (modeled as vesicles), where the symmetry breaking was induced by a large difference in the active surface tension between the two vesicles [30]. In our system the symmetry breaking is spontaneous, and the two vesicles have identical properties.

### Rigidity-dependent biting, pushing and engulfing

Next we explore the process of engulfment that mimics the phagocytosis of a non-rigid object by a cell. The engulfed (target) object is described by a small vesicle ( $N^T = 847$  vertices, forming a spherical object with radius of  $10 l_{\text{min}}$ ), and the cell-like (bigger) vesicle has 3127 vertices. We set the CMC concentration  $\rho = 4.8\%$  on the cell-like vesicle throughout this work. We start by validating our computation, demonstrating that for a very rigid target vesicle (bending modulus  $\kappa = 2000 k_B T$ ) the engulfment proceeds in the same manner as we previously computed for a perfectly rigid sphere (Fig.S6, and see SI section S8) [8]. Note that by increasing the bending modulus we rigidify the target vesicle against shape deformations that increase local mean curvature, but explicit membrane tension and area fluctuations are unaffected.

We start exploring how a cell-like vesicle that contains passive CMC ( $F = 0$ , Fig.3A), engulfs a target vesicle of different bending modulus. We find that the cell-like vesicle with passive CMC is able to fully engulf the target vesicle, with the engulfment proceeding faster for the

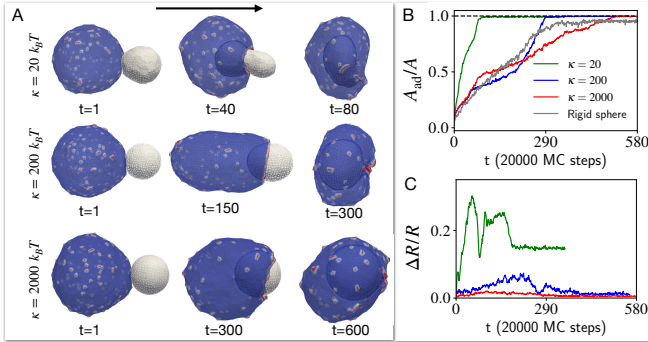


FIG. 3. The engulfment of target vesicles of different rigidities by a cell-like vesicle with passive CMC. A) The snapshots of the shapes of the interacting vesicles with time for different bending rigidity  $\kappa$  values of the target vesicle. We set the bending rigidity of the cell-like vesicle at  $20k_B T$ . B) The time evolution of adhered area fraction of the target vesicle for different  $\kappa$  values (see SI section S4 for details on this calculation). As  $\kappa$  increases, the outcome is approaching the completely rigid  $\kappa = \infty$  limit that is shown in grey. C) Time evolution of the deviation of the target vesicle from a spherical shape, for different values of  $\kappa$  (color code as in (B)), measured by the relative standard deviation for the position vector of all the vertices with respect to the center of mass of the vesicle (Eq.S11). As  $\kappa$  increases, the target remains spherical all the time, and it takes longer time to engulf as it requires the cell-like vesicle to extend its adhesion cup over a bigger cross-section.

softest target vesicle (See Movie S1). This faster engulfment is facilitated by the large deformation (See SI section S9 for details of deformation measurement) of the target vesicle (as shown in Fig.3B,C, Fig.S7B), which enables the cell-like vesicle to extend an adhesion cup over a smaller cross-sectional area.

This behaviour is drastically changed when the CMC induce active protrusive forces. We explore in Fig.4 the engulfment dynamics as function of the bending modulus  $\kappa$  of the target vesicle, and find three main dynamical phases. We start with the high  $\kappa$  regime (blue traces in Fig.4A, and blue region on the phase diagram Fig.4B), where the cell-like vesicle completely engulfs the rigid target vesicle (similar to the engulfment of a rigid object, Fig.S6 [8]), as shown in the snapshots of Fig.4E. For a softer target vesicle (green traces in Fig.4A, and green region on the phase diagram Fig.4B), we find that the target vesicle ends up being pushed away (Fig.4D), and the contact area stalls in a “suction-cup”-like shape, and later retracts (Fig.4A) until the two vesicles detach (zero final adhered area fraction, Fig.4B) due to the high bending energy of the elongated “finger” attached to the target vesicle (Fig.S8, See SI section S10). At even lower values of  $\kappa$  (red traces in Fig.4A, and red region on the phase diagram Fig.4B) we find that the engulfed area stalls at a small value ( $A_{ad}/A < 0.5$ , Fig.4A,B), corresponding to a “biting”-type dynamics (Fig.4C). Note that we do not allow the vesicles to undergo fission, even when greatly deformed.

The origin of these dynamical phases can be understood when we investigate how the membrane shape and the orientation of the active forces are coupled. In Fig.5(A) we define the components of the active force that is exerted by a CMC of the cell-like vesicle when its in contact with the nodes of the target vesicle. This force is applied towards the outwards normal of the CMC, and has both normal ( $F_{\perp}$ ) and tangential ( $F_{\parallel}$ ) components with respect to the target vesicle node.

During the engulfment phase of rigid target vesicles we find that the CMC form large leading-edge clusters (large value of the total transmitted force, blue traces in Fig.5B) which mostly exert tangential forces (Fig.5G,J). This is shown in the snapshots of Fig.5M. The average fraction of the two force components (beyond the transient initial cup formation stage, denoted by the bold lines in Fig.5B), is shown in Fig.5C, and clearly demonstrate the relation between these force components and the resulting three dynamical phases.

In the pushing phase of slightly softer target vesicles we find that the leading-edge cluster gets arrested at a smaller size (green traces in Fig.5B), eventually disappearing when the two vesicles disengage. The dynamics of the force components (Fig.5F,I) show that the normal component remains relatively high, preventing the efficient spreading of the engulfing membrane over the target vesicle. In Fig.5L the snapshots show the origin of this behavior: due to the deformation of the target vesicle, the leading-edge of the engulfing membrane is not tangentially oriented, further pushing into the target vesicle and maintaining its deformation. This feedback between shape and force orientation arrests the spreading, as the target vesicle is pushed and deformed.

In the regime of softest target vesicle (red traces in Fig.5B) the target vesicle gets strongly deformed by the adhesion to and active forces exerted by the engulfing membrane (red line in Fig.5D). This large deformation prevents the CMC and the active force from aligning tangentially, with both components having similar magnitude (Fig.5E,H). Due to the large deformations of the soft target vesicle (Fig.5K) the leading-edge ends up mostly pushing it after a small portion is engulfed, leading to a “biting”-like behavior. This is very different from the smooth engulfment observed when the active forces are absent (Fig.3).

The outcome of the engulfment process also depends on the environment, in the form of confinement and constraints on the membrane dynamics. As shown in Fig.S9, by holding a small patch of the target vesicle fixed in space, the outcome of the interaction can change from pushing to engulfment or biting (See SI section S11).

In Fig.S10 we show the same set of dynamic phases when we vary the osmotic pressure (see SI section S12 for details) inside the target vesicle (while keeping  $\kappa = 20k_B T$ ). We find that as the internal pressure  $p$  inside the target vesicle increases, the membrane of this vesicle gets stretched out and tense, inhibiting any shape changes and effectively stiffening the vesicle. Not sur-

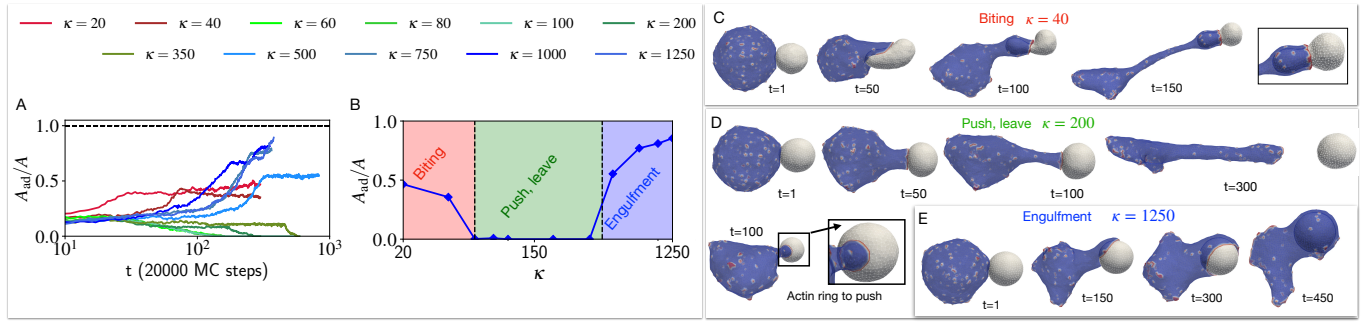


FIG. 4. Effect of the bending rigidity of the target vesicle on the process of phagocytosis. The time evolution of the adhered area fraction of the target cell is shown in (A), for different bending modulus values. B) The final adhered area fraction of the target vesicle is shown as a function of the bending rigidity  $\kappa$ . We indicated three phases of biting, push-leave, and engulfment with red green and blue as  $\kappa$  increases. The time evolution of the shapes and the snapshots are shown for three example of biting, push-leave, and engulfment in C), D) and E) panels, where the bending rigidity  $\kappa$  for the target vesicle is set to  $40 k_B T$ ,  $200 k_B T$ , and  $1250 k_B T$  respectively. We set the bending rigidity of the cell-like vesicle to  $20 k_B T$ .

prisingly, the observed phases, as function of the pressure  $p$  (Fig.S10), perfectly match the phases observed as function of bending rigidity in Fig.4.

### Comparison to experiments

We start by comparing the engulfment of a relatively rigid sphere ( $\kappa = 750 k_B T$ ), in experiments utilizing elastic beads [19, 31] and simulations (Fig.6). Note that we are limited to relatively high values of  $\kappa$  in the simulations in order to ensure engulfment (Fig.4). In the experiments the actin recruitment is highly localized to the leading edge of the engulfing membrane, in agreement with our association of the actin force with the highly curved CMC cluster in the simulations. A band of normal force exerted by this leading edge on the engulfed sphere results in local squeezing of the sphere, in both experiments and simulations. The localization of the squeezing force and the shape deformation are more pronounced in the experiments compared to our simulations. This may arise due to the shell-like description of the engulfed sphere in the simulations, while it is a fully filled elastic bead in the experiments. There may also be additional contractile forces exerted by the cell at the leading edge, which we do not currently describe in our model. Nevertheless, the overall agreement is good.

Note that at the bead's pole pointing at the engulfing cell the experiment measures a pulling force acting on the bead, which may arise from contractile forces pulling on these adhesion sites, or due to the effect of actin treadmilling emanating from the leading edge, exerting forces that pinch the bead at this pole (similar to actin treadmilling-induced forces that are involved with endocytosis [32]). This effect is absent from our simple model. We also observe that the actin at the leading edge is non-uniform and fragmented in both the experiments and our simulations, suggesting that a simple coupling between curvature and actin nucleation may be involved

in a complex and non-uniform organization of this moving front [33, 34].

Experiments found lower rates of successful engulfment for soft beads [17, 19], in agreement with our simulation results (Fig.4).

In Fig.7 we compare the theoretical predictions of three dynamical phases as function of the membrane tension of the target vesicle, to experimental observations. Fig.7(A-C) gives examples of snapshots of the interactions between macrophage cells (labeled in green) and giant unilamellar vesicles that contain antibodies that trigger macrophage adhesion (GUVs, labeled in pink) [20]. In the experiments the membrane tension was varied using different sucrose solutions to fill the GUVs, and as function of decreasing membrane tension the observed behavior changes from (mostly) engulfment at high tension (Fig.7A), to a mixture of pushing and some biting at intermediate tensions (Fig.7B), finally exhibiting biting (trogocytosis) activity for the lowest GUV membrane tensions (Fig.7C, See Movies S2, S3, S4).

In Fig.7(D-F) we show examples of a macrophage (green) interacting with a lymphoma cell (magenta). From top to bottom we see the same three typical behaviors: engulfment (Fig.7D), pushing (Fig.7E) and biting (trogocytosis, Fig.7F) (See Movies S5, S6, S7 respectively). While we do not know exactly the stiffness of each of these cancer cells, finding this range of behaviors and comparing to our model suggests that cancer cells exhibit a wide range of stiffness [35]. This trait of cancer cells was indeed measured using Atomic Force Microscopy (AFM) [36, 37].

In Fig.7(G-I) we demonstrate how the three phases observed in the experiments are predicted by our theoretical simulations as a function of the pressure inside the engulfed target vesicle (See Movies S8, S9, S10, respectively). Higher internal pressure acts to suppress dynamic changes and fluctuations in the target vesicle's area, equivalent to higher membrane tension (Fig.S11). Note that we do not allow our vesicles to undergo topo-

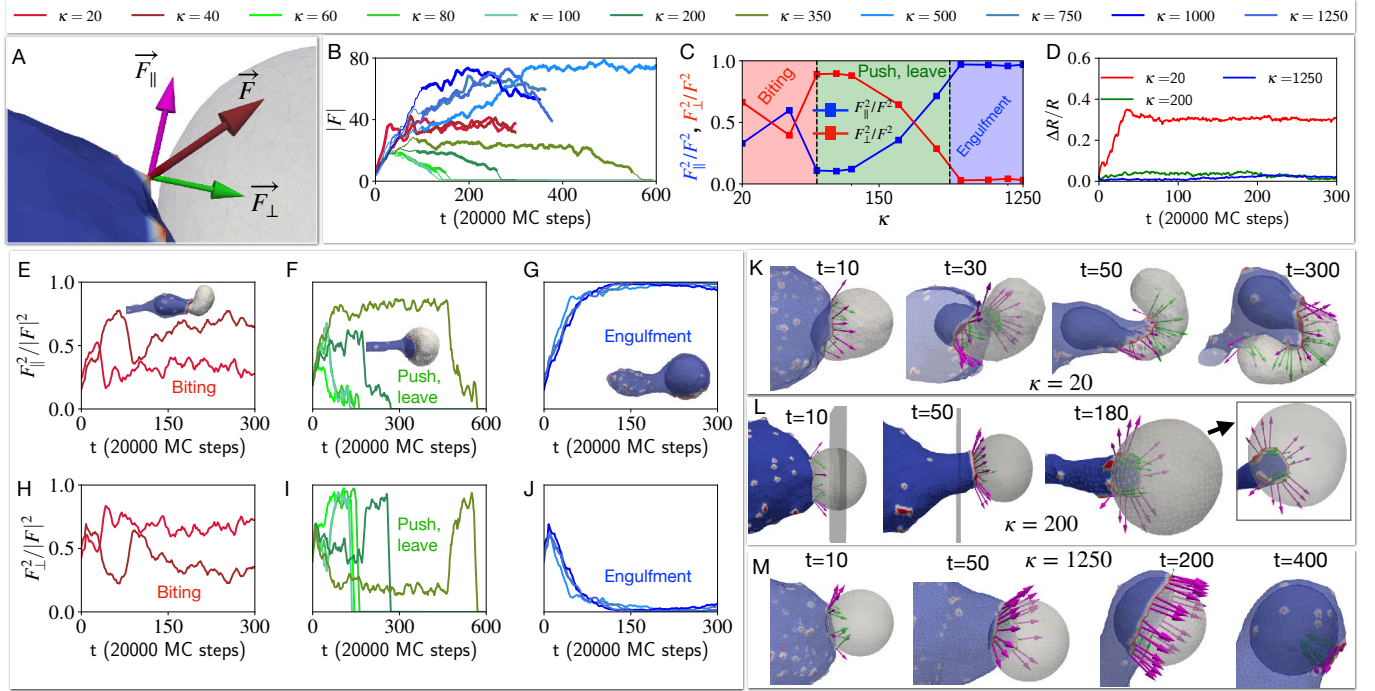


FIG. 5. Coupling between the target vesicle deformation and alignment of the active forces during the engulfment process. A) The active force due to an active CMC node of the cell-like vesicle is applied to a neighboring node of the target vesicle  $\vec{F}$ . This force is decomposed into two parts,  $\vec{F}_{\parallel}$  is tangential to the surface of the target vesicle and  $\vec{F}_{\perp}$  is the pushing normal force (shown in magenta and green colour, respectively). B) The time evolution of the total magnitude of the force applied to the target vesicle by the cell-like vesicle is shown, for different bending rigidities of the target vesicle (as in Fig.4). C) Time averaged the tangential and normal force fractions as function of the bending rigidity of the target vesicle  $\kappa$  (over the times denoted by bold lines in (B)). D) The deviation of the target vesicle from a sphere is shown for three different bending rigidities  $\kappa$  of the target vesicle (Eq.S11). E-G) show the fraction of tangential force on the target in the three dynamical regimes of biting, push-leave, and engulfment. H-j) Similarly, the fraction of normal pushing force on the target in the three dynamical phases. K)-M) Snapshots showing the force decomposed into tangential and normal components together with the deformations of the target vesicle. We show how the early deformation caused by the normal components affect the later alignment of the CMC at the leading edge of the adhesion patch. K) A very soft target vesicle can initially adhere and bend into the cell-like vesicle, during the early stages. However, the CMC then impinge against the remaining target vesicle, and end up pushing and twisting it with a significant normal component. L) In the pushing regime the deformation of the target vesicle is sufficient to prevent the CMC from aligning tangentially, and a significant normal component maintains the pushing dynamics. M) For the rigid target vesicle the CMC cluster aligns tangentially and drives efficient engulfment. The bending rigidity of the bigger cell is set to  $20k_B T$ .

logical changes such as fission, so the biting behaviour in the simulations is arrested.

Our model also offers an explanation to the puzzling observations of cells either engulfing or pushing away apoptotic cells during embryogenesis [38]. Similar to our simulations, cells were observed to push away some apoptotic cells, and eventually detach from them, as we calculate (Fig.4D). We propose that the engulfed cells in this system are either stiffer, or happen to be confined by neighboring cells (Fig.S9).

## DISCUSSION

We have explored here the dynamics of cellular adhesion and engulfment of soft objects, whereby the mech-

anism of the self-organization of the protrusive forces of actin polymerization is through curved membrane protein complexes (CMC). Curved membrane proteins that recruit actin polymerization were shown to drive cellular protrusions during cell adhesion and migration [11, 13, 14]. This mechanism was previously shown to explain how cells phagocytose rigid objects [8], and here we explored this mechanism when the engulfed object is flexible.

Our model predicts that as function of the stiffness or membrane tension of the engulfed vesicle, there are distinct dynamical phases: While a stiff object is engulfed, a softer object will be spontaneously pushed away until it detaches. The softest objects get partially engulfed, which we expect in reality to result in a piece getting "bitten" off (trogocytosis). The theoretical model ex-

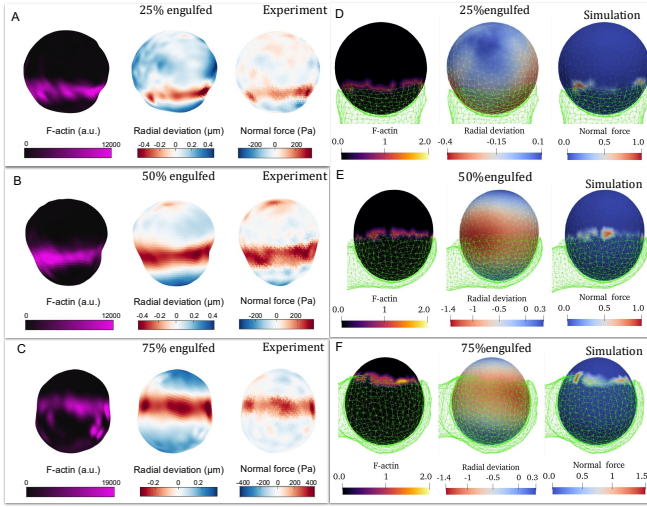


FIG. 6. A-C) 3D reconstructions of deformable acrylamide-co-acrylic acid-microparticles (DAAM-particles) (1.4 kPa, 9  $\mu\text{m}$ ) revealing F-actin over the particle surface, detailed target deformations induced during phagocytosis and normal forces inferred from shape deformations. DAAM-particles were functionalized with Immunoglobulin G (IgG) and stained with TAMRA-cadaverine and exposed to phagocytosis by RAW264.7 cells, which were then fixed and stained for F-actin. Each panel displays (left) F-actin distribution across the particle surface, (middle) radial deformation, and (right) the normal traction forces inferred from the shape deformations. (D-F) Snapshots of the simulated target vesicle (relatively rigid,  $\kappa = 750k_B T$ ) at different values of engulfment (green transparent network denotes the engulfing cell-like membrane). Heatmaps show the location of the CMC (left), target vesicle radial deformation (middle) and the normal component of the active force exerted by the CMC on the target vesicle (right). These correspond to the actin localization in the experiments, bead deformation and normal elastic forces, respectively. The reconstructions in A, B and C correspond to the same engulfment percentages shown in D, E and F, respectively.

plains the origin of these dynamical phases as arising due to the feedback between the deformations of the engulfed object, and the orientation of the active forces exerted by the cell's leading edge. Comparing to experiments of immune cells engulfing artificial vesicles or cancer cells, we validate the predicted relation between engulfment dynamics and the mechanical deformability of the target.

Note that our model predicts that successful engulfment of soft targets is facilitated by the cell employing weaker cytoskeletal forces (Fig.3). Altogether, these results suggest possible future interventions to enhance or inhibit phagocytosis and trogocytosis based on the interplay between the target's stiffness and the protrusive activity of the engulfing cell.

Our model is using only the most minimal physical components and forces, and therefore offers a path to obtaining deep and general understanding of an important biological process which is shared by many cell types [39-41]. Future extensions of our modeling approach could

include additional processes, such as myosin-induced contractility and the effects of actin treadmilling-induced forces, in addition to more complex description of the adhesion between the cell and its target (which may itself depend on stiffness and applied forces [20]).

## I. METHODS AND MATERIAL

**Lipids**—Phosphocholine (PC) lipids (Avanti Polar Lipids) were used as purchased without further purification. Lipid stock solutions in chloroform contained a ternary mixture of 98 mol% POPC, 1 mol% biotin-PE, and 1 mol% PEG2K DSPE. GUVs are diluted in an ionic solution of PBS and all lipids in our mixtures are zwitterionic. We added PEG2K DSPE to block GUVs from aggregating in the charge-screened PBS solution.

**Antibodies**—Antibodies used to opsonize GUVs were purchased from Santa Cruz Biotechnology and used without further labeling or purification. Biotin was bound by AlexaFluor647-labeled anti-biotin mouse IgG (clone BK-1/39, Santa Cruz Biotechnologies).

**RAW 264.7 cell culture**—RAW 264.7 murine male macrophage-like cell line was obtained from and authenticated by the UC Berkeley Cell Culture Facility. Cells were cultured in RPMI 1640 media (Corning) supplemented with 10% heat-inactivated fetal bovine serum (HI-FBS, Thermo Fisher Scientific) and 1% Pen-Strep (Thermo Fisher Scientific). RAWs were cultured in non-tissue culture-treated 10 cm dishes (VWR) at 37°C, 5%  $\text{CO}_2$ .

**Stable LifeAct GFP RAW 264.7 cell line**—HEK293T cells were grown in a 6-well plate to 80% confluence, and 160 ng VSV-G, 1.3  $\mu\text{g}$  CMV 8.91, and 1.5  $\mu\text{g}$  target pH LifeAct GFP expression vector were transfected into HEK293T cells using TransIT-293T transfection reagent (Mirus Bio). Viral supernatants were collected 60 hours after transfection and spun at 4000 G to remove HEK293T cells. Viral supernatant was stored at 4°C for no longer than 48 hours prior to infection. For lentiviral infection, 500  $\mu\text{L}$  of viral supernatant was added to 5e5 RAW 264.7 macrophages along with 4  $\mu\text{g}/\text{mL}$  polybrene, and cells were spun at 400G for 25 minutes at 37°C and then resuspended and plated in a 6-well plate. Viral media was replaced with fresh growth media 24 h after infection. Cells were sorted via fluorescence-activated cell sorting on an Influx Cell Sorter (Beckton-Dickinson), and a population of cells expressing LifeAct GFP was expanded and frozen for later use.

**GUV electroformation**—Solutions containing 0.25 mg total lipids were spread evenly on slides coated with indium tin oxide (70-100  $\Omega/\text{sq}$ ; Sigma Aldrich). The slides were placed under vacuum for >30 min to allow

for complete evaporation of chloroform. A capacitor was created by sandwiching a 0.3-mm rubber septum between two lipid-coated slides. The gap was filled with 200  $\mu\text{L}$  of 300 mM sucrose (hyperosmotic solution compared to PBS (285 mOsm) to make high-tension GUVs) or 270 mM sucrose (hypoosmotic solution compared to PBS to make low-tension GUVs). Sucrose solution osmolarity was measured using an osmometer (Precision Systems). GUVs 10 to 100  $\mu\text{m}$  in diameter were electroformed by application of an AC voltage of 1.5 V at 10 Hz across the capacitor for 1 h at 55°C.

**Imaging techniques**—All live cells were maintained at 37°C, 5%  $\text{CO}_2$  with a stage top incubator (Okolab) during imaging. For confocal microscopy, cells were imaged with a spinning disk confocal microscope (Eclipse Ti, Nikon) with a spinning disk (Yokogawa CSU-X, Andor), sCMOS camera (Prime 95B, Photometrics), and a 60x objective (Apo TIRF, 1.49NA, oil, Nikon). The spinning disk confocal microscope was controlled with Nikon Elements (Nikon). Images were analyzed and prepared using FIJI (imagej.net/software/fiji).

**Phagocytosis/trogocytosis of GUVs**—50,000 macrophages were seeded in wells of an 8-well glass-bottom plate (CellVis) in 100  $\mu\text{L}$  of RPMI 1640 medium. Post-seeding, cells were incubated at 37°C, 5%  $\text{CO}_2$  for 3-4 hours before target addition. 100  $\mu\text{L}$  of low-tension GUVs or high-tension GUVs (1 million GUVs counted with an impedance-based cell counter (Scepter, SigmaAldrich)) were prepared with 4  $\mu\text{M}$  AlexaFluor647 anti-biotin IgG in PBS and allowed to incubate with gentle rotation for > 10 minutes. After washing, GUVs were added to macrophage-seeded wells on the stage top incubator of the microscope.

**Time-lapse confocal microscopy of antibody-dependent cellular phagocytosis** — J774A.1 macrophages and Raji B lymphocytes were obtained from DSMZ (ACC170, ACC319). J774A.1 that stably express Lifeact-mScarlet31 [42] were cultured at 37°C with 5%  $\text{CO}_2$  in DMEM (Wisent, 319-005) supplemented with 10% of heat-inactivated FBS (Wisent, 090-150). Raji were cultured were cultured at 37°C with 5%  $\text{CO}_2$  in RPMI-1640 (Wisent, 350-007) supplemented with 10% of heat-inactivated FBS (Wisent, 090-150). 24 hours before imaging, 100,000 macrophages were seeded into 18 mm circular #1.5 coverslips. Prior to the experiment, Raji cells were stained with Calcein AM viability dye (eBioscience, 65-0853-78) at 1  $\mu\text{M}$  for 30 minutes. Macrophages were transferred to a Chamlide CMB imaging chamber (Live Cell Instrument) and incubated in DMEM without phenol red, containing 25 mM HEPES (Wisent, 319-066). 200,000 Raji cells were added to the macrophages, and 2  $\mu\text{g}/\text{ml}$  of anti-human CD20 antibody (BioXcell, Rituximab) and 10  $\mu\text{g}/\text{ml}$  of anti-human CD47 antibody (BioXcell, B6.H12) were supplemented. Images were acquired every 20 seconds

for 2 hours using a 40x 1.3 NA oil immersion objective on a Nikon Eclipse Ti2-E, equipped with a Yokogawa SCU-W1 spinning disk, a Hamamatsu Orca-Fusion BT sCMOS camera, and a stage-top incubator (Tokai Hit) to maintain cells at 37°C. Images were acquired using Nikon NIS Elements and analyzed using Fiji is just ImageJ 1.54p.

**Microparticle traction force microscopy (MP-TFM) analysis of phagocytosis of DAAM-particles**— Experimental data was obtained from prior conducted experiments [43] in which RAW 264.7 macrophages were exposed to IgG-functionalized 1.3 kPa deformable poly-Aam-co-AAc microparticles (DAAM-particles), stained for F-actin using Alexa Fluor-488 conjugated phalloidin, and imaged by confocal microscopy [44]. DAAM-particle 3D shape reconstructions and force analysis were performed as previously described [18, 45]. Briefly, the inverse problem of inferring the traction forces  $\mathbf{T}$  is solved iteratively until a minimal gradient tolerance is reached. During this optimization, an ideal sphere with the same particle volume of the measured individual particle is subjected to a trial displacement field ( $\mathbf{u}$ ) to exactly match the surface of the experimentally observed shape of the DAAM-particle, while minimizing the cost function:

$$f(\mathbf{u}) = E_{el} + \alpha R^2(T; \partial\Omega_t) + \beta E_{pen}(T) \quad (3)$$

where  $R(T; \partial\Omega_t)$  represents the residual cellular forces exerted outside of the cell-target contact region, defined from the phalloidin and immunostaining. The elastic energy ( $E_{el}$ ) penalizes unphysical solutions in which larger forces producing the same shape, while  $\beta E_{pen}$  serves as an anti-aliasing term. The weighing parameters,  $\alpha$ (residual traction) and  $\beta$ (anti-aliasing), were both set to 1. Spherical harmonic coefficients up to  $l_{max} = 20$  were utilized and normal forces were evaluated on a 21  $\times$  41 grid.

**Interaction between the vesicles**—Two vesicles were left to interact through adhesion. The adhesive energy per node between two vesicles is set to  $E_{ad} = 2k_B T$ . If the vertices from different vesicles come within the interaction range (set to  $l_{min}$ ) then this adhesive energy is taken into account. The process is passive when the interaction is solely through the adhesion between them, and there is no active force imparted on the target vesicle by the bigger cell-like vesicle. An active force is imparted by a CMC node in the cell-like vesicle on a vertex in the target vesicle. To calculate the tangential and normal force imparted, we calculate the interaction force first. Let  $V_i$  be the vertex of interest in the target vesicle, and  $\hat{n}_i$  be its outward normal (computed by taking the average of the normals for all the triangles having the vertex in common). The normal and tangential components of the interaction force due to the sum of active forces act-

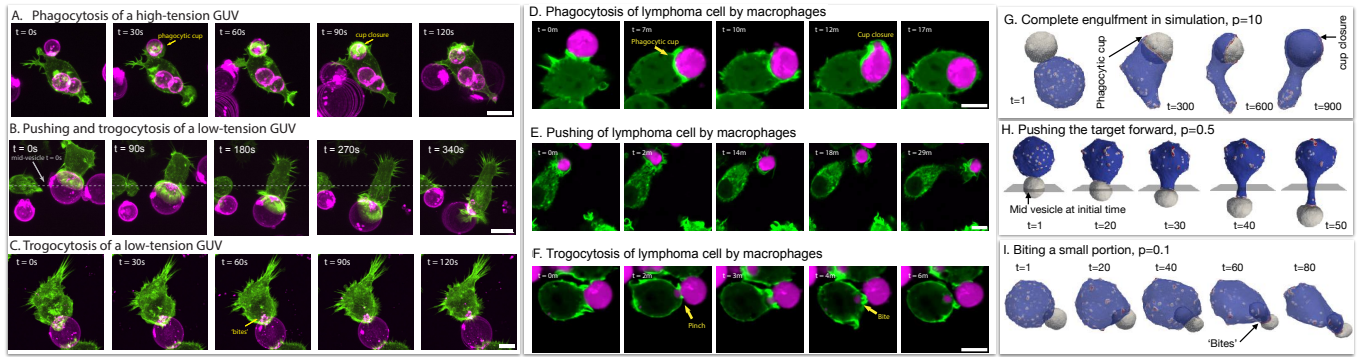


FIG. 7. (A) Giant unilamellar vesicles (GUVs) composed of POPC and biotin-DOPE and filled with a hyperosmotic sucrose solution (300 mOsm), leading to taut high-tension vesicles, are opsonized with AlexaFluor647 anti-biotin and mixed with LifeAct-GFP-expressing macrophages. During phagocytosis, the macrophage forms a phagocytic cup, identifiable from enriched actin in a ring, that encircles the GUV. The macrophage fully engulfs the GUV within tens of seconds. (B) GUVs filled with a hypoosmotic sucrose solution (270 mOsm) are at low tension and can be ‘pushed’ by a macrophage, as shown by the position of the vesicle over time relative to the mid-plane at  $t=0$ s. (C) When low-tension GUVs are trogocytosed by a macrophage, punctate ‘bites’ can be observed within the macrophage. Scale bar is 5  $\mu$ m. (D-F) Time-lapse confocal microscopy images show interactions between macrophages (Lifeact-mScarlet3, pseudo-colored in green) and antibody-opsonized lymphoma cells (pseudo-colored in magenta). (D) Example of a macrophage engulfing an entire target cell. (E) Example of a macrophage pushing the target cell. (F) Example of a macrophages trogocytosing a fragment of the target cell. Scale bars are 10  $\mu$ m. In simulations, (G) the complete engulfment of the target vesicle when its osmotic pressure is high  $p = 10 k_B T l_{\min}^{-3}$ . (H) The target is pushed when the osmotic pressure is intermediate  $p = 0.5 k_B T l_{\min}^{-3}$ . A plane that is shown perpendicular to the pushing direction through the middle of the target vesicle’s initial position. (I) For a very low osmotic pressure,  $p = 0.1 k_B T l_{\min}^{-3}$ , the cell-like vesicle takes a bite from the target.

ing on this vertex,  $\mathbf{F}_i$ , are given by,

$$\begin{aligned}\mathbf{F}_\perp &= (\mathbf{F}_i \cdot \hat{n}_i) \hat{n}_i, \\ \mathbf{F}_\parallel &= \mathbf{F}_i - (\mathbf{F}_i \cdot \hat{n}_i) \hat{n}_i.\end{aligned}\quad (4)$$

For a more detailed description, see SI sections S1-S3 and the methods and material.

**Setup for the engulfment simulation**— In all the simulations of the engulfment process, we construct two vesicles: i) a big cell-like vesicle with 3127 vertices, out of which 150 vertices represent the curved proteins with intrinsic mean curvature  $c_0 = 1l_{\min}^{-1}$ , the protein-protein interaction energy is set to  $w = 1 k_B T$ , and ii) a smaller target vesicle made of 847 vertices with no curved proteins. At the initial time, the two vesicles were nearly spherical in shape and placed very near to each other, within the adhesion distance. The bending rigidity for the cell-like vesicle is set to  $20k_B T$  throughout the paper. We varied the bending rigidity of the target vesicle from  $20k_B T$  to a very high value of  $2000k_B T$ , which is nearly a rigid sphere.

## II. CODE AVAILABILITY

The MATLAB code for analyzing confocal images and deriving particle shape is publicly available on [https://gitlab.com/dvorselen/DAAMparticle\\_Shape\\_Analysis](https://gitlab.com/dvorselen/DAAMparticle_Shape_Analysis). The Python code for traction force analysis is available on [https://gitlab.com/micronano\\_public/ShElastic](https://gitlab.com/micronano_public/ShElastic).

## ACKNOWLEDGMENTS

N.S.G. is the incumbent of the Lee and William Abramowitz Professorial Chair of Biophysics, and acknowledges support by the Israel Science Foundation (Grant No. 207/22). This research is made possible, in part, by the historic generosity of the Harold Perlman Family. This work is supported by a National Science Foundation (NSF) Centre for Cellular Construction grant DBI-1548297 (to D.A.F.), National Institutes of Health (NIH) grant R01GM134137 (to D.A.F.) and Chan Zuckerberg Biohub Investigator (to D.A.F.). It was also supported by the James S. McDonnell Foundation Postdoctoral Fellowship (to C.E.C.). The authors A.I. and S.P. acknowledge the financial support from the Slovenian Research Agency (ARIS) for the research project J3-60063 and programme P2-0232, the EU Horizon 2020 Research and Innovation Programme under the Marie Skłodowska-Curie Staff exchange project “FarmEVs” (grant agreement no: 101131175) and EU project COST-CA22153.

**Author contributions**— SS, NSG designed the computational model and research. SS developed the code and performed the simulations and data analysis. CEC, DAF performed the experiments with GUVs and phagocytes. MKS, VJ performed the experiments with the lymphoma cells and phagocytes. YP, DV performed the experiments with DAAM particles. AI, SP developed the original single vesicle code. NSG, SS wrote the manuscript, and all the authors edited the manuscript.

[1] R. S. Flannagan, V. Jaumouillé, and S. Grinstein, The cell biology of phagocytosis, *Annual Review of Pathology: Mechanisms of Disease* **7**, 61 (2012).

[2] E. Uribe-Querol and C. Rosales, Phagocytosis: our current understanding of a universal biological process, *Frontiers in immunology* **11**, 1066 (2020).

[3] J. A. Swanson, Shaping cups into phagosomes and macropinosomes, *Nature reviews Molecular cell biology* **9**, 639 (2008).

[4] S. Mylvaganam, S. A. Freeman, and S. Grinstein, The cytoskeleton in phagocytosis and macropinocytosis, *Current Biology* **31**, R619 (2021).

[5] A. K. Panah and V. Jaumouillé, Signaling of phagocytosis, in *Encyclopedia of Immunobiology (Second Edition)*, edited by P. M. Kaye (Academic Press, Oxford, 2026) second edition ed., pp. 651–669.

[6] D. Vorselen, R. L. D. Labitigan, and J. A. Theriot, A mechanical perspective on phagocytic cup formation, *Current opinion in cell biology* **66**, 112 (2020).

[7] V. Jaumouillé and C. M. Waterman, Physical constraints and forces involved in phagocytosis, *Frontiers in immunology* **11**, 1097 (2020).

[8] R. K. Sadhu, S. R. Barger, S. Penič, A. Iglič, M. Krendel, N. C. Gauthier, and N. S. Gov, A theoretical model of efficient phagocytosis driven by curved membrane proteins and active cytoskeleton forces, *Soft Matter* **19**, 31 (2023).

[9] G. Scita, S. Confalonieri, P. Lappalainen, and S. Suetegu, Irspl53: crossing the road of membrane and actin dynamics in the formation of membrane protrusions, *Trends in cell biology* **18**, 52 (2008).

[10] J. Linkner, G. Witte, H. Zhao, A. Junemann, B. Nordholz, P. Runge-Wollmann, P. Lappalainen, and J. Faix, The inverse bar domain protein ibara drives membrane remodeling to control osmoregulation, phagocytosis and cytokinesis, *Journal of Cell Science* **127**, 1279 (2014).

[11] I. Begemann, T. Saha, L. Lamparter, I. Rathmann, D. Grill, L. Golbach, C. Rasch, U. Keller, B. Trappmann, M. Matis, *et al.*, Mechanochemical self-organization determines search pattern in migratory cells, *Nature Physics* **15**, 848 (2019).

[12] A. Pipathsouk, R. M. Brunetti, J. P. Town, B. R. Graziano, A. Breuer, P. A. Pellett, K. Marchuk, N.-H. T. Tran, M. F. Krummel, D. Stamou, *et al.*, The wave complex associates with sites of saddle membrane curvature, *Journal of Cell Biology* **220**, e202003086 (2021).

[13] M. Wu, R. K. Sadhu, K. Meyer, Z. Tang, P. Marchando, D. N. Woolfson, N. S. Gov, and O. D. Weiner, Wave complex forms linear arrays at negative membrane curvature to instruct lamellipodia formation, *Journal of Cell Biology* **224**, e202410098 (2025).

[14] R. K. Sadhu, A. Iglič, and N. S. Gov, A minimal cell model for lamellipodia-based cellular dynamics and migration, *Journal of Cell Science* **136**, jcs260744 (2023).

[15] R. K. Sadhu, M. Luciano, W. Xi, C. Martinez-Torres, M. Schröder, C. Blum, M. Tarantola, S. Villa, S. Penič, A. Iglič, *et al.*, A minimal physical model for curvotaxis driven by curved protein complexes at the cell's leading edge, *Proceedings of the National Academy of Sciences* **121**, e2306818121 (2024).

[16] S. Sadhukhan, C. Martinez-Torres, S. Penič, C. Beta, A. c. v. Iglič, and N. Gov, Modeling how lamellipodia-driven cells maintain persistent migration and interact with external barriers, *Phys. Rev. Res.* **7**, 013319 (2025).

[17] K. A. Beningo and Y.-l. Wang, Fc-receptor-mediated phagocytosis is regulated by mechanical properties of the target, *Journal of cell science* **115**, 849 (2002).

[18] D. Vorselen, Y. Wang, M. M. de Jesus, P. K. Shah, M. J. Footer, M. Huse, W. Cai, and J. A. Theriot, Microparticle traction force microscopy reveals subcellular force exertion patterns in immune cell-target interactions, *Nature Communications* **11**, 10.1038/s41467-019-13804-z (2020).

[19] A. H. Settle, B. Y. Winer, M. M. de Jesus, L. Seeman, Z. Wang, E. Chan, Y. Romin, Z. Li, M. M. Miele, R. C. Hendrickson, *et al.*,  $\beta 2$  integrins impose a mechanical checkpoint on macrophage phagocytosis, *Nature Communications* **15**, 8182 (2024).

[20] C. E. Cornell, A. Chorlay, D. Krishnamurthy, N. R. Martin, L. Baldauf, and D. A. Fletcher, Target cell cortical tension regulates macrophage trogocytosis, *Nature Cell Biology* , 1 (2025).

[21] K. R. Rollins, S. Fiaz, I. Datta, and M. A. Morrissey, Target cell adhesion limits macrophage phagocytosis and promotes trogocytosis, *Journal of Cell Biology* **224**, e202502034 (2025).

[22] J. Shen, X. Li, G. Hide, Z.-R. Lun, and Z. Wu, Trogocytosis: revealing new insights into parasite–host interactions, *Trends in Parasitology* (2025).

[23] M. Fošnarič, S. Penič, A. Iglič, V. Kralj-Iglič, M. Drab, and N. S. Gov, Theoretical study of vesicle shapes driven by coupling curved proteins and active cytoskeletal forces, *Soft Matter* **15**, 5319 (2019).

[24] R. K. Sadhu, S. Penič, A. Iglič, and N. S. Gov, Modelling cellular spreading and emergence of motility in the presence of curved membrane proteins and active cytoskeleton forces, *The European Physical Journal Plus* **136**, 495 (2021).

[25] J. Pavlič, T. Mareš, J. Bešter, V. Janša, M. Daniel, and A. Iglič, Encapsulation of small spherical liposome into larger flaccid liposome induced by human plasma proteins, *Computer Methods in Biomechanics and Biomedical Engineering* **12**, 147 (2009).

[26] C. Tordeux, J.-B. Fournier, and P. Galatola, Analytical characterization of adhering vesicles, *Physical Review E* **65**, 041912 (2002).

[27] M. Frank, M. Manček-Keber, M. Kržan, S. Sodin-Šemrl, R. Jerala, A. Iglič, B. Rozman, and V. Kralj-Iglič, Prevention of microvesiculation by adhesion of buds to the mother cell membrane—a possible anticoagulant effect of healthy donor plasma, *Autoimmunity Reviews* **7**, 240 (2008).

[28] T. Mareš, M. Daniel, A. Iglič, V. Kralj-Iglič, and M. Fošnarič, Determination of the strength of adhesion between lipid vesicles, *The Scientific World Journal* **2012**, 146804 (2012).

[29] J. Urbanija, B. Babnik, M. Frank, N. Tomšič, B. Rozman, V. Kralj-Iglič, and A. Iglič, Attachment of  $\beta 2$ -glycoprotein i to negatively charged liposomes may prevent the release of daughter vesicles from the parent membrane, *European Biophysics Journal* **37**, 1085 (2008).

[30] A. Torres-Sánchez, M. Kerr Winter, and G. Salbreux, Interacting active surfaces: A model for three-dimensional cell aggregates, *PLOS Computational Biology* **18**, e1010762 (2022).

[31] D. Vorselen, Y. Wang, M. M. de Jesus, P. K. Shah, M. J. Footer, M. Huse, W. Cai, and J. A. Theriot, Microparticle traction force microscopy reveals subcellular force exertion patterns in immune cell–target interactions, *Nature communications* **11**, 20 (2020).

[32] F. Motahari and A. Carlsson, Actin based pulling forces in endocytosis, *Biophysical Journal* **112**, 561a (2017).

[33] J. C. Herron, S. Hu, T. Watanabe, A. T. Nogueira, B. Liu, M. E. Kern, J. Aaron, A. Taylor, M. Pablo, T.-L. Chew, *et al.*, Actin nano-architecture of phagocytic podosomes, *Nature communications* **13**, 4363 (2022).

[34] K. Sopelniak, R. Batlouni, Q.-f. Sun, P. Cervero, and S. Linder, Phagocytic podosomes enable efficient uptake of *candida auris* by primary human macrophages, *bioRxiv* , 2025 (2025).

[35] C. Rianna, M. Radmacher, and S. Kumar, Direct evidence that tumor cells soften when navigating confined spaces, *Molecular biology of the cell* **31**, 1726 (2020).

[36] M. Lekka, Discrimination between normal and cancerous cells using afm, *Bionanoscience* **6**, 65 (2016).

[37] M. Yang, Y. Yang, L. Liu, and M. Li, Single-cell parallel plate mechanics by side-view optical microscopy-assisted atomic force microscopy, *Nanoscale Advances* **7**, 2158 (2025).

[38] E. Hoijman, H.-M. Häkkinen, Q. Tolosa-Ramon, S. Jimenez-Delgado, C. Wyatt, M. Miret-Cuesta, M. Iríomia, A. Callan-Jones, S. Wieser, and V. Ruprecht, Cooperative epithelial phagocytosis enables error correction in the early embryo, *Nature* **590**, 618 (2021).

[39] K. Miyake and H. Karasuyama, The role of trogocytosis in the modulation of immune cell functions, *Cells* **10**, 1255 (2021).

[40] D. Vorselen, Dynamics of phagocytosis mediated by phosphatidylserine, *Biochemical Society Transactions* **50**, 1281 (2022).

[41] S. Barbera, M. J. Schuiling, N. A. Sanjaya, I. Pietilä, T. Sarén, M. Essand, and A. Dimberg, Trogocytosis of chimeric antigen receptors between t cells is regulated by their transmembrane domains, *Science immunology* **10**, eado2054 (2025).

[42] T. W. Gadella Jr, L. Van Weeren, J. Stouthamer, M. A. Hink, A. H. Wolters, B. N. Giepmans, S. Aumonier, J. Dupuy, and A. Royant, mscarlet3: a brilliant and fast-maturing red fluorescent protein, *Nature methods* **20**, 541 (2023).

[43] D. Vorselen, S. Barger, J. Theriot, N. Gauthier, and M. Krendel, Phagocytic microscopy and mp-tfm assay with raw macrophages upon treatment with cytoskeletal inhibitors (2021).

[44] D. Vorselen, S. R. Barger, Y. Wang, W. Cai, J. A. Theriot, N. C. Gauthier, and M. Krendel, Phagocytic ‘teeth’ and myosin-ii ‘jaw’ power target constriction during phagocytosis, *eLife* **10**, 10.7554/elife.68627 (2021).

[45] A. Mali, Y. Peeters, R. Rodrigues de Mercado, A. H. Settle, M. J. Footer, M. Srinivas, J. A. Theriot, and D. Vorselen, Using tunable hydrogel microparticles to measure cellular forces, *Nature Protocols* 10.1038/s41596-025-01281-2 (2025).

# Supplementary material: From biting to engulfment: curvature–actin coupling controls phagocytosis of soft, deformable targets

Shubhadeep Sadhukhan,<sup>1,\*</sup> Caitlin E. Cornell,<sup>2</sup> Mansehaj Kaur Sandhu,<sup>3</sup> Youri Peeters,<sup>4</sup> Samo Penič,<sup>5</sup> Aleš Iglič,<sup>5</sup> Daniel A. Fletcher,<sup>2,6,7,8</sup> Valentin Jaumouillé,<sup>3</sup> Daan Vorselen,<sup>4</sup> and Nir S. Gov<sup>1,9,†</sup>

<sup>1</sup>*Department of Chemical and Biological Physics, Weizmann Institute of Science, Rehovot, Israel*

<sup>2</sup>*Department of Bioengineering, University of California Berkeley; Berkeley, CA USA*

<sup>3</sup>*Department of Molecular Biology and Biochemistry, Simon Fraser University, Burnaby BC, Canada*

<sup>4</sup>*Department of Cell Biology and Immunology, Wageningen University and Research, Wageningen, the Netherlands*

<sup>5</sup>*Laboratory of Physics, Faculty of Electrical Engineering, University of Ljubljana, Ljubljana, Slovenia*

<sup>6</sup>*University of California Berkeley/University of California San Francisco Graduate Group in Bioengineering, CA USA*

<sup>7</sup>*Division of Biological Systems and Engineering,  
Lawrence Berkeley National Laboratory; Berkeley CA USA*

<sup>8</sup>*Chan Zuckerberg Biohub; San Francisco CA USA*

<sup>9</sup>*Department of Physiology, Development and Neuroscience,  
Downing Site, University of Cambridge, Cambridge, UK*

(Dated: January 29, 2026)

## S1. THEORETICAL MODEL

We modelled the cell membrane as a three-dimensional vesicle which is described by a closed surface with  $N$  vertices connected to its neighbours by bonds and it forms a dynamically triangulated, self-avoiding network, with the topology of sphere [4, 5].  $\mathbf{r}_i$  is the position vector of the  $i$ th vertex. All the lengths are measured in a scale of  $l_{\min}$ . There is a percentage  $\rho = 100N_c/N$  of vertex sites that represent the curved membrane protein complexes (CMC), that induce cytoskeletal active forces. The vesicle energy has four components: The bending energy is given by,

$$W_b = \frac{\kappa}{2} \int_A (C_1 + C_2 - C_0)^2 \, dA, \quad (S1)$$

where,  $\kappa$  is the bending rigidity,  $C_1, C_2$  are the principal curvatures and  $C_0$  is the spontaneous curvature. We consider the spontaneous curvature  $C_0 = 1l_{\min}^{-1}$  for the CMC sites, represented in red and blue represents the bare membrane for which  $C_0 = 0$ . The protein-protein interaction energy is given by,

$$W_d = -w \sum_{i < j} \mathcal{H}(r_0 - r_{ij}) \quad (S2)$$

where  $\mathcal{H}$  is the Heaviside function,  $r_{ij} = |\mathbf{r}_i - \mathbf{r}_j|$  is the distance between protein sites,  $r_0$  is the range interaction and  $w$  is the strength. We set the parameter  $w = 1k_B T$  throughout the paper. The energy due to the active force is given by,

$$W_F = -F \sum_i \hat{n}_i \cdot \mathbf{r}_i \quad (S3)$$

where  $F$  is the magnitude of the active force,  $\hat{n}_i$  is the outward unit normal vector of the  $i$ th protein site vertex and  $\mathbf{r}_i$  is the position vector of the protein.

Finally, the adhesion energy due to an adhesive rigid substrate is given by,

$$W_A = - \sum_i E_{ad} \quad (S4)$$

where  $E_{ad}$  is the adhesion strength, and the sum runs over all the adhered vertices to the substrate i.e., the vertices that are within a range of  $1l_{\min}$ .

\* shubhadeep.sadhukhan@weizmann.ac.il

† nir.gov@weizmann.ac.il

## S2. DETECTION OF OTHER VESICLES

We always started the vesicles are well separated in space, i.e., not intersecting each other. In multi-vesicle simulation, it is important to make sure that one vertex of a vesicle is not going into the other vesicles during the vertex move. If we pick a vertex from a vesicle that is very close to another vertex that belongs to other vesicle, then we check whether the vesicle is cutting the other vesicle. We need to check any such pair of vertices from different vesicles. Let the vertex of interest  $\mathcal{V}_1$  (with which we want to make a Monte-Carlo (MC) vertex movement step), is very close to another vertex  $\mathcal{V}_2$ , then we exploit the information of tristar associated with the vertex  $\mathcal{V}_2$ . We have  $T_2$  as the "tristar" (a list of triangles, see Fig. S1) associated with  $\mathcal{V}_2$ . The  $i$ th triangle of the tristar  $T_2$  is presented by  $T_{2i}$ . Let  $\vec{r}_1$  and  $\vec{r}_2$  be the position vectors of  $\mathcal{V}_1$  and  $\mathcal{V}_2$  respectively. We calculate the projection of the relative position of  $\mathcal{V}_1$  with respect to  $\mathcal{V}_2$  that is  $\vec{r}_{12} = \vec{r}_1 - \vec{r}_2$  on the normals  $\hat{n}_i$  of each triangles  $T_{2i}$  as follows:

$$p_i = \vec{r}_{12} \cdot \hat{n}_i = (\vec{r}_1 - \vec{r}_2) \cdot \hat{n}_i \quad (S5)$$

where  $i$  runs through all the triangles in the tristar list  $T_2$  of vertex  $\mathcal{V}_2$ . If any  $p_i$  becomes negative, it means the vertex  $\mathcal{V}_1$  intersected the triangle  $T_{2i}$ . Hence, we abort that vertex movement.

## S3. VESICLE-VESICLE INTERACTION

Two vesicles can interact with each other through adhesion and impart the active force due to the actin-cytoskeleton.

**Vesicle-vesicle adhesion**—Two different vesicles can adhere to each other. Let  $E_{ad}$  be the adhesive energy per node for cell-cell adhesion. The interaction between two vesicles through adhesion becomes effective only when the two vesicles come very close and within a finite range of adhesion  $1l_{\min}$ . Therefore, if a vertex of vesicle 1 comes within the range of cell-cell adhesion of any of the vertices belonging to another vesicle (say vesicle 2), then we count  $E_{ad}$  as the cell-cell adhesion energy in the energy calculation of the vertex of interest that belongs to the vesicle 1 (See Fig.1D).

**Force applied on the other vesicle**—A vesicle can impart active force on the other vesicle. If a vertex is within the range of interaction (The interaction range is set to  $1l_{\min}$ ) of other protein vertices belonging to the other vesicle, a vectorially added effective force is applied on the former vertex. If a set  $\mathcal{S}$  of vertices belongs to another vesicle are within the interaction range of a vertex of interest  $\mathcal{V}_i$  then the force applied on the vertex  $\mathcal{V}_i$  is given by,

$$F = \sum_{V_i \in \mathcal{S}} F_{V_i} \quad (S6)$$

Let the vertex of interest  $\mathcal{V}_1$  (with which we want to make a vertex movement step), is very close to another vertex  $\mathcal{V}_2$  then we exploit the information of list of neighboring triangles associated with the vertex  $\mathcal{V}_2$ . Let say  $T_2$  is tristar (a list of triangles See Fig. S1) associated with  $\mathcal{V}_2$ . The  $i$ th triangle of the tristar  $T_2$  is presented by  $T_{2i}$ . Let  $\vec{r}_1$  and  $\vec{r}_2$  be the position vectors of  $\mathcal{V}_1$  and  $\mathcal{V}_2$  respectively. We calculate the projection of the relative position of  $\mathcal{V}_1$  with respect to  $\mathcal{V}_2$  that is  $\vec{r}_{12} = \vec{r}_1 - \vec{r}_2$  on the normals  $\hat{n}_i$  of each triangles  $T_{2i}$  as follows:

$$p_i = \vec{r}_{12} \cdot \hat{n}_i = (\vec{r}_1 - \vec{r}_2) \cdot \hat{n}_i \quad (S7)$$

where  $i$  runs through all the triangles in the tristar list  $T_2$  of vertex  $\mathcal{V}_2$ . If any  $p_i$  become negative it means the vertex  $\mathcal{V}_1$  intersected the triangle  $T_{2i}$ . Hence, we abort that vertex movement.

The interaction between the vesicles is mediated by the active forces applied by the others vesicles. Any vertex feels the active force due to the other vesicle's active protein sites. The effect of interaction force is included by adding the energy cost due to the interaction force given by,

$$W_{\text{int}} = \vec{F}^{\text{int}} \cdot \vec{dr} = \sum_i F_i \cdot \vec{dr} \quad (S8)$$

where  $i$  runs through all the vertices belonging to other vesicles but within the distance of  $l_{\min}$  from the vertex of interest.

## S4. CALCULATION OF ADHERED AREA FRACTION OF THE TARGET VESICLE

To calculate the adhered area fraction of the target vesicle, we used a simple method by counting the number of nodes that are in the vicinity of the nodes of other vesicles and dividing it by the total number of nodes. We calculate

it for different cases as follows:

**Adhesive area fraction calculation for the triangulated vesicle**— To calculate the adhesion area fraction, we scan through all the vertices of a vesicle to check if the vertex is within the adhesion range from any other vesicle or the adhesive substrate. If the vertex is within the adhesion range to any other adhesive surface, then we count it as an adhered vertex. Finally, we find the approximate adhesive area fraction by dividing the number of adhered vertices  $N_{\text{ad}}$  by the total number of vertices  $N$ .

**Adhesion fraction calculation for rigid sphere**— We do not have the information for the vertices for the case of a rigid sphere. To make a similar calculation to the calculation used in the vesicle with a triangulated membrane, we generated 847 vertex points (same as the number of vertices on the target vesicle) on the sphere using a Fibonacci lattice.

Let's say, we shall place  $N^T$  number of vertices on a sphere of radius  $R$ , centred at  $(x_0, y_0, z_0)$  using the Fibonacci lattice. We shall generate  $N^T$  points given by,

$$\begin{aligned} x_i &= x_0 + R \left( 1 - \frac{2(i-1)}{(N^T - 1)} \right) \\ y_i &= y_0 + \sqrt{(R^2 - x_i^2)} \sin \phi \\ z_i &= z_0 + \sqrt{(R^2 - x_i^2)} \cos \phi \end{aligned} \quad (\text{S9})$$

where,  $\phi = \pi(3 - \sqrt{5})$  is the golden angle and the integer index  $i$  runs from 1 to  $N^T$ . We placed 847 points on a sphere of radius  $10 l_{\text{min}}$ . Then, we do the same calculation as before.

## S5. VERIFICATION OF RADIUS OF CURVATURE NEAR THE CONTACT WITH A SINGLE VESICLE

A single vesicle is allowed to spread on a flat adhesive substrate (Fig. S2A). After getting to the steady state, we calculated the contact angle when the area and the volume of the vesicle are conserved. It can be theoretically estimated from the energy terms if there are no curved proteins and no active forces. Theoretically, the radius of curvature is given by  $R = \sqrt{\kappa/2E_{\text{ad}}}$  [2]. We analyzed a two-dimensional cross-section of the vesicle shape, let's say  $x - z$  plane as shown in Fig. S2A. Then, we approximately identified the contact region and then fit a circle of radius  $R$  that gives the radius of curvature near the contact point, as shown in Fig. S2B. Since the numerical results may fluctuate, we have found the value of  $R$  by taking an average of the fit after rotating the vesicle about the  $z$  axis as it has rotational symmetry about the  $z$  axis. We took ten realizations by rotating the vesicle in steps of  $36^\circ$ . We can estimate an error by taking the statistical error bar.

One can find the contact angle  $\theta_c$  by fitting the straight line near the contact as shown in Fig. S2B. We did a similar angular averaging to calculate the contact angle.

A single vesicle is allowed to spread on an adhesive substrate for different adhesion energy  $E_{\text{ad}}$  parameters and different CMC densities  $\rho = 0, 3.46\%, 6.93\%$ . The shapes for all these different cases when the total volume of the vesicle is conserved are shown in Fig. S3A. We showed the case when the vesicle volume is not conserved in Fig. S3B. We have shown the steady-state adhered area fraction for all these cases in Fig. S3C. There is a higher adhered area fraction when the adhesive energy  $E_{\text{ad}}$  per node is higher. We also see that the curved-protein percentage is driving the spreading, by reducing the bending energy cost near the contact line. When the volume is not conserved, we find that the vesicle can lose its volume to assume a sheet-like shape and spread more, as shown in Fig. S3C.

We have shown the two-dimensional side cut of the vesicle on  $x - z$  plane and the fitted circle in order to calculate the radius of curvature in lime (See Fig. S3D). We verified the radius of curvature  $R$  for  $E_{\text{ad}} = 1k_B T$  and  $2k_B T$  when volume is conserved and the curved proteins are absent as shown in Fig. S3E. The theoretical estimation is given by the grey solid line.

## S6. VERIFICATION OF RADIUS OF CURVATURE NEAR THE CONTACT WITH TWO IDENTICAL VESICLES

Next, we consider two identical vesicles that adhere to each other. Again, we find the radius of curvature near the contact and validated with the previous work [2]. Though the technique to calculate the radius of curvature is similar to the case of the single vesicle, you need to orient the vesicles properly before making any observation. We first draw a straight line joining the center of mass of the two vesicles, as shown in Fig. S2C. We then align this

line to the  $z$  axis by rotation. We calculated the radius of curvature near the contact for the cases of no CMC and with volume conservation, for two different parameters for the adhesion energy  $E_{ad}$  per node. The snapshots for two vesicles spreading on each other are shown in Fig. S4A. The adhesive area fraction is increased as the adhesive energy per node is increased (See Fig. S4B). Also, the adhesion area fraction is larger in the presence of the CMC. The volume conservation hinders the spreading, with the adhered area fraction increasing with increasing CMC concentration and increasing adhesive energy  $E_{ad}$  per node.

## S7. ADHESION DYNAMICS BETWEEN TWO VESICLES WITH PASSIVE CMC AND NO VOLUME CONSERVATION

In Fig.2 we show the steady-state final shapes of two identical vesicles adhered to each other for different strengths of adhesion energy parameter  $E_{ad}$  and passive CMC. In Fig.S5 we plot the evolution of the energy terms for the two vesicles during these processes. We show that above a critical adhesion energy of  $\sim 1.2k_B T$  there is spontaneous breaking of the symmetry, with one of the vesicles experiencing a large increase in its bending energy (Fig.S5A), which is of course compensated by the large increase in the negative magnitude of the adhesion energy (Fig.2B,C). The vesicle that deforms into a cap-shape forms a ring cluster of its CMC, which indeed provides a larger interaction energy between the proteins (Fig.S5B).

## S8. BENCHMARK OF PHAGOCYTOSIS WITH A RIGID SPHERICAL PARTICLE

Next, we have two non-identical vesicles and let them interact through adhesion, and the active forces that mimic the actin cytoskeleton. One vesicle is bigger in size and contains CMC, representing a cell-like vesicle. The other vesicle is smaller in size and has no CMC for simplicity, serving as the target-vesicle. We kept the bending rigidity of the cell-like vesicle  $\kappa = 20k_B T$  throughout the paper. Therefore, whenever we talk about the bending rigidity  $\kappa$  in the context of the phagocytosis process, it is the bending rigidity of the target vesicle.

Before we explore the complex behaviours exhibited by the very soft objects due to their big deformations, we validate the model by comparing two cases: We consider a completely rigid spherical object as a target [3], and compare the dynamics to the case of a very rigid target (high bending rigidity  $\kappa = 2000k_B T$ ) vesicle of the same radius. We simulate these two cases with a model cell-like vesicle containing wither passive ( $F = 0k_B T l_{\min}^{-1}$ ) or active ( $F = 2k_B T l_{\min}^{-1}$ ) CMC.

We find the adhered area fraction is very similar for the completely rigid object and the target vesicle with very high bending rigidity  $\kappa = 2000k_B T$  for both the passive and active cases, respectively, as shown in Fig. S6E-F. We have also found that the active vesicle is more efficient in complete engulfment compared to the passive vesicle, as shown in Fig. S6G. We have shown the different stages of the engulfment processes with snapshots of the interaction between two vesicles in Fig. S6A-D for four different cases.

## S9. VESICLE AREA DEFORMATION AND FLUCTUATIONS DURING PASSIVE ENGULFMENT

In Fig.3 we show the engulfment of vesicles of different bending rigidities by cell-like vesicle that contains passive CMC. The engulfment involves deformations of the target vesicle, which are quantified as follows: First, we find the centroid  $\vec{r}_0$  of the vesicle by averaging the position vectors of all the vertices. Next, we find the distances of all the vertices from the centroid that is given by,

$$\tilde{r}_i = |\vec{r}_i - \vec{r}_0|. \quad (\text{S10})$$

Next, we find the relative standard deviation of these distances  $r_i$  is given by,

$$\Delta R/R = \sqrt{\langle \tilde{r}_i^2 \rangle - \langle \tilde{r}_i \rangle^2} / \langle \tilde{r}_i \rangle. \quad (\text{S11})$$

A sphere has a non-roundedness measure of zero, and it increases as the vesicle becomes more non-spherical.

The non-roundness parameter for the target vesicle is shown in Fig.3C. Similarly, changes to the vesicle's area during this engulfment process are shown in Fig.S7.

## S10. DETACHMENT OF THE CELL-LIKE VESICLE FROM THE TARGET AFTER A PUSHING EVENT

In Fig.4D we showed that for intermediate target vesicle rigidities the cell-like vesicle ends up pushing it. This process ends with the cell-like vesicle detaching from the target vesicle and retracting the long protrusion that formed. In Fig.S8 we plot the bending energies of the two vesicles during this process, and the sum of the adhesion and protein-protein interaction energy for the cell-like vesicle. We see that as the pushing event progresses, there is an increase in the bending energy associated with the long protrusion of the cell-like vesicle ( $E_{b1}$  in Fig.S8), while the adhesion and protein-protein binding energies which compensate for it decrease. This increasing energy cost eventually drives the detachment, and retraction, which decreases the bending energy cost.

## S11. EFFECT OF HOLDING THE TARGET ON THE ENGULFMENT PROCESS

We have found that in the regime of intermediate rigidity, the cell-like vesicle pushes the target vesicle and ultimately leaves it without biting or engulfing it (Fig. S9A, Fig.4D). Here we simulated the dynamics when an external constraint confines the target vesicle. For example, in an "in vitro" experiment a target may be held by a pipette [1], or cells may be confined by surrounding cells inside tissues.

To mimic such a confinement effect, we designated a patch of vertices on the target vesicle that are not allowed to move. We choose a patch of vertices centered at the pole of the target vesicle away from the cell-like vesicle (black patch on the right-most edge of the target vesicle in Fig. S9B). This is a patch of depth of  $l_{\min}$  from the pole of the target vesicle. We found that this confinement can change the dynamics from pushing to engulfment or biting (trophocytosis), as shown in Fig. S9B and see the Movie S11.

We showed how different quantities, such as the adhered area fraction, deformation, tangential force fraction and normal force fraction evolve over MC steps as shown in Fig. S9C. Holding a patch of the target vesicle changes the entire engulfment dynamics by directing more of the active force to be tangential to the target vesicle, therefore much more efficient in driving engulfment.

## S12. EFFECT OF INTERNAL PRESSURE OF THE TARGET CELL

When an osmotic pressure difference  $p$  exists between the inside and the outside of the target vesicle, an additional energy cost term is included [?],

$$\Delta E_p = pdV \quad (S12)$$

Here,  $dV$  is the change in volume due to the Monte Carlo moves (e.g. vertex movement, bond flip). The positive internal pressure  $p$  creates more tension on the membrane, and the vesicle gets inflated.

We have systematically studied the effect of the internal osmotic pressure of the target vesicle on the engulfment process, while keeping the bending rigidity of the target-like vesicle at  $\kappa = 20k_B T$ . We found three dynamical phases (Fig. S10), identical to the phases found for varying the bending rigidity (Fig.4). As the internal pressure increases, the target vesicle membrane is under higher tension, which opposes the deformation and keeps it more spherical. Increasing internal osmotic pressure in the target vesicle therefore affects the engulfment process in an identical way to increasing the bending rigidity of the target vesicle (Fig.4).

We next calculated a measure of the membrane tension due to the internal osmotic pressure  $p$ , as shown in Fig.S11. As both the volume and area of the vesicle are changing, we introduced the volume-normalized area  $\tilde{A}$  given by,

$$\tilde{A} = \frac{A}{V^{2/3}} \quad (S13)$$

where,  $A$  and  $V$  are the area and the volume of the vesicle. The time evolution of  $\tilde{A}$  is shown in Fig. S11A for the cases of internal pressures of  $p = 0.1, 0.5$  and  $10$ , during the interaction of the target with an active cell-like vesicle (as in Fig.7G-I). Next, we calculated the probability distribution of the volume-normalized area  $\rho(\tilde{A})$  (Fig.S11B). As pressure increases, the distribution function has a very narrow and sharp peak. A sharper peak implies a lower standard deviation  $\sigma_{\tilde{A}}$  of the area fluctuations for higher internal pressure  $p$  as shown in Fig. S11C. Lower area fluctuations are equivalent to higher membrane tension.

**Movie S1: Passive engulfment of the soft vesicle:**— The cell-like vesicle with passive ( $F = 0$ ) curved protein

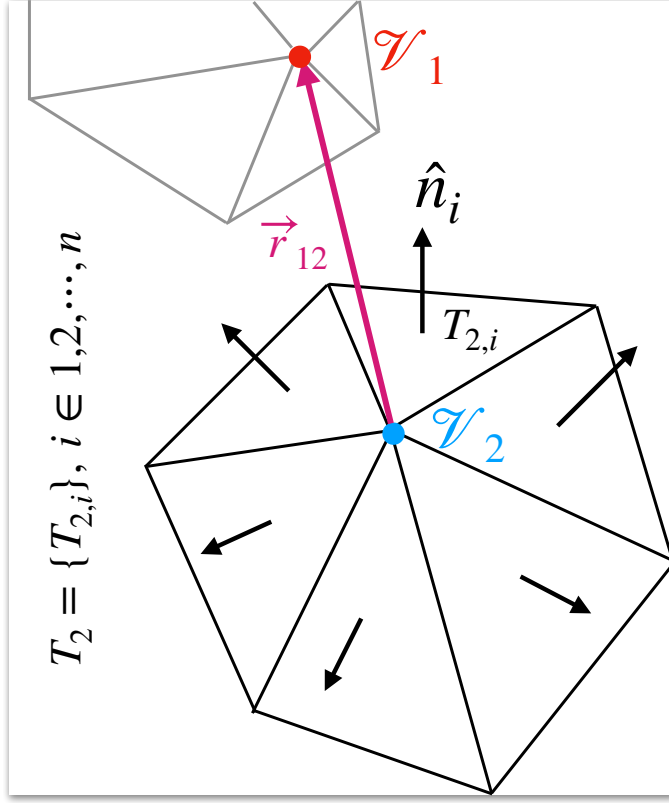


FIG. S1. Demonstration of the detection of an overlap between two vesicles. Two vertices  $\mathcal{V}_1$  and  $\mathcal{V}_2$  belong to two different vesicles separated by the position vector  $\vec{r}_{12}$ . We check a MC change to the position of the vertex  $\mathcal{V}_1$ , given that the vector  $\vec{r}_{12}$  magnitude is less than the minimum length scale  $l_{\min}$ . Keeping the vertex  $\mathcal{V}_2$  at the center, the neighbouring triangles create a triangle list denoted by the set  $T_2$ . We check the dot product of the normals of the member triangles with the position vector  $\vec{r}_{12}$ . If any of the dot products is negative, then the two vesicles are overlapping.

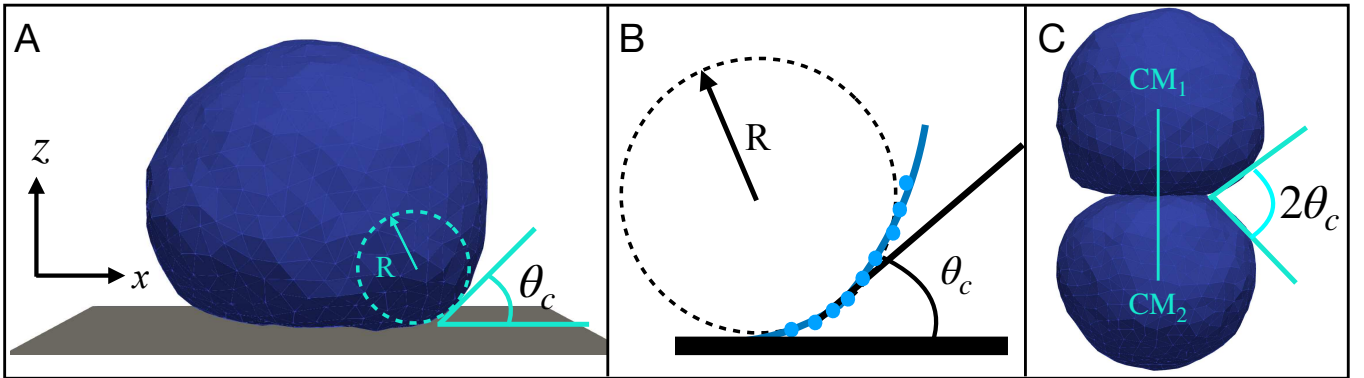


FIG. S2. (A) A vesicle is adhered on an adhesive substrate. We find the cross section of the vesicle on the  $x - z$  plane. Near the adhesion region we find the radius of curvature  $R$ . We find the angle of contact by making a linear fit with the points near the contact line: (B) Here, the relevant points along the vesicle surface are shown in blue dots. They are used to make a circular fit to find  $R$ , and the linear fit to find the contact angle  $\theta_c$ . (C) For two vesicles adhering to each other, first we join their centers of mass ( $CM_1$  and  $CM_2$ ) and align it along  $z$  direction. Then we applied the same procedure to find  $R$  and  $\theta_c$  as in (B). As the system has rotational symmetry around the  $z$ -direction, we averaged over 10 cases by rotating the system in steps of  $36^\circ$  around the  $z$  direction.

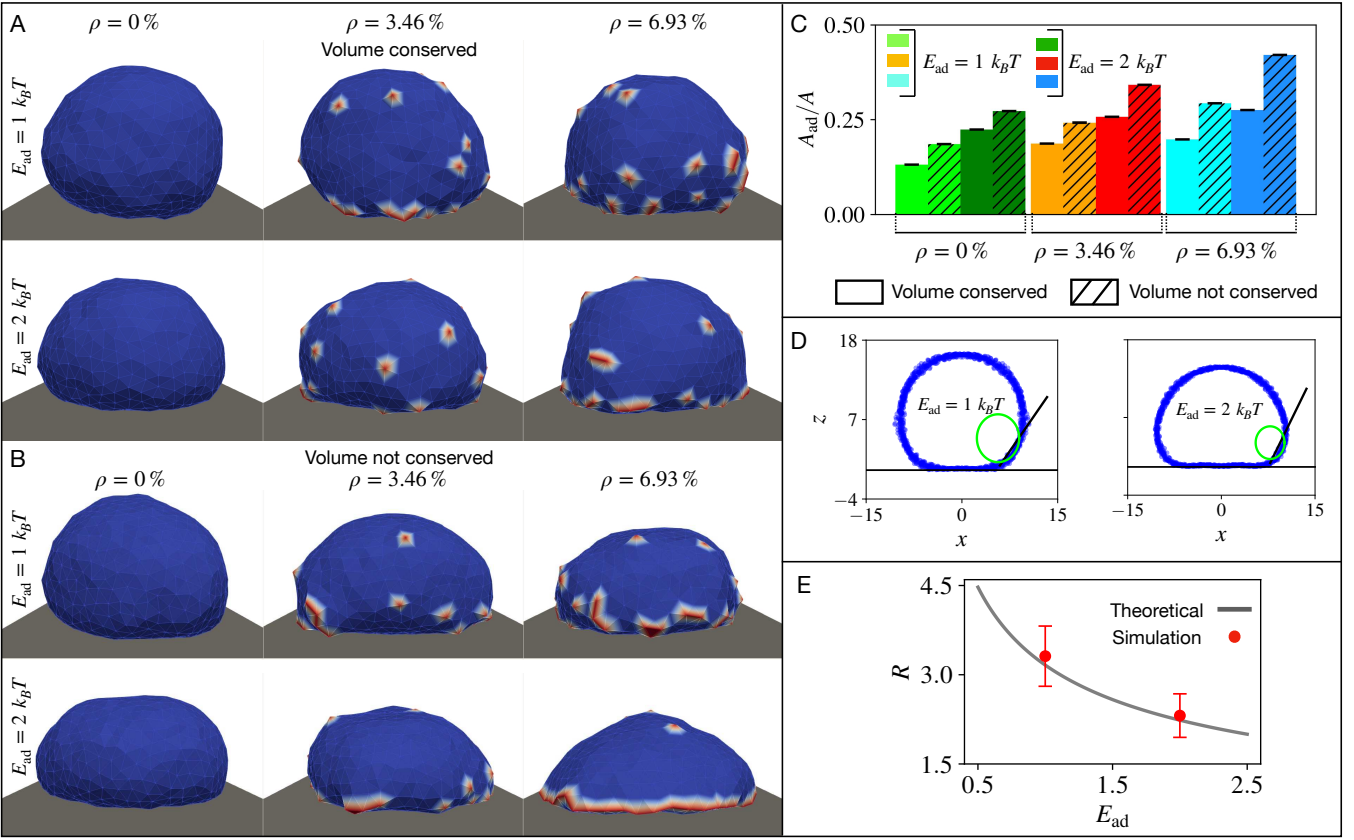


FIG. S3. Verification of the radius of curvature near the contact line of a vesicle on the flat substrate. A) Snapshots of the vesicle adhering to the flat substrate when the volume and the area are conserved, for different concentrations of CMC (passive) and adhesion energies. B) Same as (A) when the volume conservation constraint is removed. C) Adhered area fraction is shown as a bar plot for different cases shown in (A,B). D) Numerical extraction of the radius of curvature near the substrate-vesicle contact line from the simulated shapes. E) Verification of the predicted dependence of the radius of curvature (as defined in Fig.S2) on the adhesion energy [2] for two cases of  $E_{ad} = 1 k_B T$ ,  $2 k_B T$ , when there are no CMC ( $\rho = 0\%$ ) and the volume is conserved.

engulfing the target vesicle. We set the parameters for a cell-like vesicle  $N = 3127$ ,  $\kappa = 20 k_B T$ ,  $\rho = 4.8\%$ ,  $c_0 = 1 l_{min}^{-1}$ ,  $w = 1 k_B T$ . The parameters for a target vesicle are set as  $N = 847$ ,  $\kappa = 20 k_B T$ ,  $\rho = 0\%$ . The adhesive energy between the cell-like vesicle and the target vesicle is  $E_{ad} = 2 k_B T$ .

**Movie S2: (Experiment) GUV is engulfed by the macrophage**—Macrophages phagocytose taut GUVs. The macrophage cytosol is labeled by CellTracker Green CMFDA, and the actin is labeled by LifeAct GFP (green). The GUV is opsonized with fluorescent anti-biotin AlexaFluor 647 (magenta). Each frame is 30 seconds.

**Movie S3: (Experiment) GUV is pushed by the macrophage**—Macrophages push and then phagocytose low-tension GUVs. The macrophage cytosol is labeled by CellTracker Green CMFDA, and the actin is labeled by LifeAct GFP (green). The GUV is opsonized with fluorescent anti-biotin AlexaFluor 647 (magenta). Each frame is 30 seconds.

**Movie S4: (Experiment) GUV is bitten by the macrophage**—Macrophages phagocytose low-tension GUVs. The macrophage cytosol is labeled by CellTracker Green CMFDA, and the actin is labeled by LifeAct GFP (green). The GUV is opsonized with fluorescent anti-biotin AlexaFluor 647 (magenta). Each frame is 30 seconds.

**Movie S5: (Experiment) Lymphoma cell is engulfment by the macrophage**—The example of phagocytosis of a lymphoma cell (magenta) by a lifeact-expressing macrophage (green). Time stamp hours:minutes: seconds.

**Movie S6: (Experiment) Lymphoma cell is pushed by the macrophage**—The example of a lifeact-expressing macrophage (green) pushing a lymphoma cell (magenta). Time stamp hours:minutes: seconds.

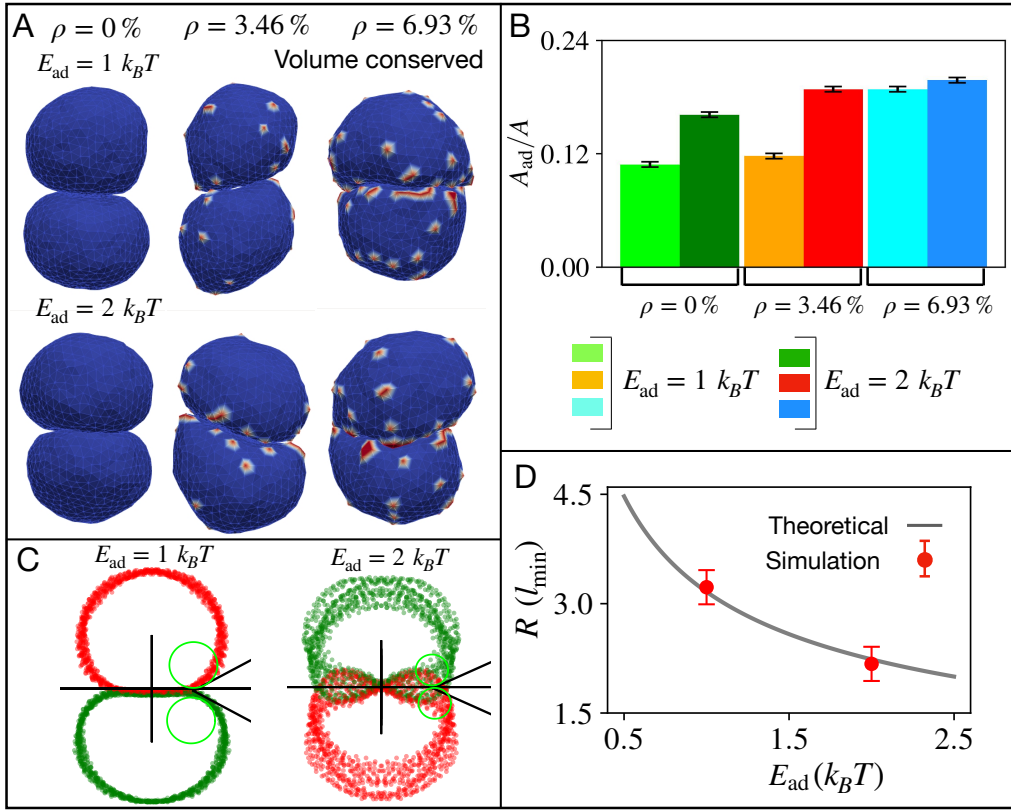


FIG. S4. Verification of radius of curvature near the contact line of two adhered symmetric vesicles when the volume and area are kept constant. A) Snapshots of two vesicles adhering to each other for three different CMC densities ( $\rho = 0\%, 3.46\%,$  and  $6.93\%$ ), and different adhesion energies  $E_{ad} = 1 k_BT, 2 k_BT$ . B) The adhered area fraction is shown as a bar plot. C) The numerical calculation of the radius of curvature near the contact line between the two adhered vesicles for the case of  $\rho = 0\%$ . D) Comparison of the numerical estimates of the radius of curvature compared with the theoretical prediction  $R_{th} = \sqrt{\frac{\kappa}{2E_{ad}}}$  shown in grey line. We used the number of vertices  $N = 722$ ,  $\kappa = 20 k_BT$ ,  $w = 1 k_BT$ ,  $c_0 = 1 l_{min}^{-1}$  for both vesicles.

**Movie S7: (Experiment) Lymphoma cell got bitten by the macrophage**—The example of trogocytosis/biting of a lymphoma cell (magenta) by a lifeact-expressing macrophage (green). Time stamp hours:minutes:seconds.

**Movie S8: Active cell-like vesicle engulfing the target**—The cell-like vesicle with active ( $F \neq 0$ ) curved protein engulfing the target vesicle. We set the parameters for a cell-like vesicle  $N = 3127$ ,  $\kappa = 20 k_BT$ ,  $\rho = 4.8\%$ ,  $c_0 = 1 l_{min}^{-1}$ ,  $w = 1 k_BT$ ,  $F = 2k_BTl_{min}^{-1}$ . The parameters for a target vesicle are set as  $N = 847$ ,  $\kappa = 20 k_BT$ ,  $\rho = 0\%$ . The target vesicle maintains an internal osmotic pressure  $p = 10 k_BTl_{min}^{-3}$ . The adhesive energy between the cell-like vesicle and the target vesicle is  $E_{ad} = 2k_BT$ .

**Movie S9: Active cell-like vesicle pushing the target**—The cell-like vesicle with active ( $F \neq 0$ ) curved protein pushing and finally leaves the target vesicle. We set the parameters for a cell-like vesicle  $N = 3127$ ,  $\kappa = 20 k_BT$ ,  $\rho = 4.8\%$ ,  $c_0 = 1 l_{min}^{-1}$ ,  $w = 1 k_BT$ ,  $F = 2k_BTl_{min}^{-1}$ . The parameters for a target vesicle are set as  $N = 847$ ,  $\kappa = 20 k_BT$ ,  $\rho = 0\%$ . The target vesicle maintains an internal osmotic pressure  $p = 0.5 k_BTl_{min}^{-3}$ . The adhesive energy between the cell-like vesicle and the target vesicle is  $E_{ad} = 2k_BT$ .

**Movie S10: Active cell-like vesicle biting the target**—The cell-like vesicle with active ( $F \neq 0$ ) curved protein biting a portion of the target vesicle. We set the parameters for a cell-like vesicle  $N = 3127$ ,  $\kappa = 20 k_BT$ ,  $\rho = 4.8\%$ ,  $c_0 = 1 l_{min}^{-1}$ ,  $w = 1 k_BT$ ,  $F = 2k_BTl_{min}^{-1}$ . The parameters for a target vesicle are set as  $N = 847$ ,  $\kappa = 20 k_BT$ ,  $\rho = 0\%$ . The target vesicle maintains an internal osmotic pressure  $p = 0.1 k_BTl_{min}^{-3}$ . The adhesive energy between the cell-like vesicle and the target vesicle is  $E_{ad} = 2k_BT$ .

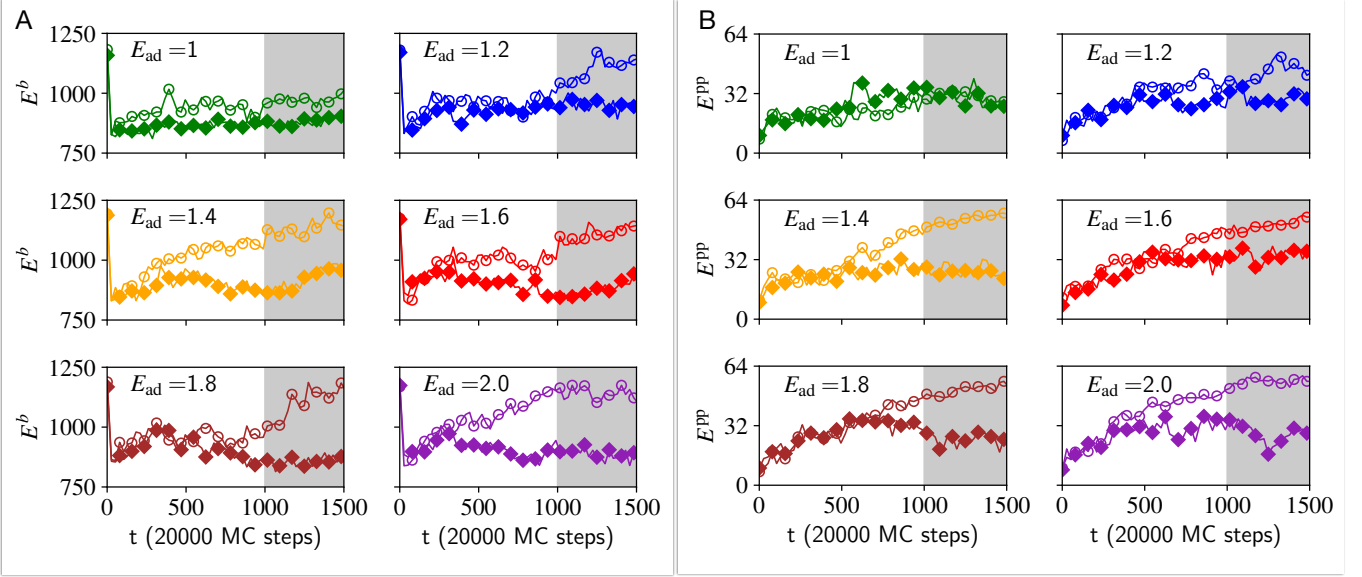


FIG. S5. Energy terms during the adhesion dynamics between two vesicles shown in Fig.2 (open symbols for the top vesicle 2, and filled symbols for the bottom vesicle 1). A) The asymmetry in the bending energies  $E^b$  for two identical vesicles without volume conservation as the adhesive energy strength increases from  $1k_B T$  to  $2k_B T$ . The bending rigidity for two vesicles is set to  $\kappa = 20k_B T$  and the protein percentage is set to  $\rho = 6.92\%$  for both vesicles. B) The asymmetry in protein-protein interaction energy  $E^{PP}$  for the same cases as in (A). Each vesicle consists of 722 vertices.

**Movie S11: Active cell-like vesicle biting the target instead of pushing, when held a patch**—The cell-like vesicle with active ( $F \neq 0$ ) curved protein biting the target vesicle instead of pushing while held a circular patch by freezing (shown in black) the vertices of the target. We set the parameters for a cell-like vesicle  $N = 3127$ ,  $\kappa = 20 k_B T$ ,  $\rho = 4.8\%$ ,  $c_0 = 1 l_{\min}^{-1}$ ,  $w = 1 k_B T$ ,  $F = 2k_B T l_{\min}^{-1}$ . The parameters for a target vesicle are set as  $N = 847$ ,  $\kappa = 200 k_B T$ ,  $\rho = 0\%$ . The adhesive energy between the cell-like vesicle and the target vesicle is  $E_{ad} = 2k_B T$ .

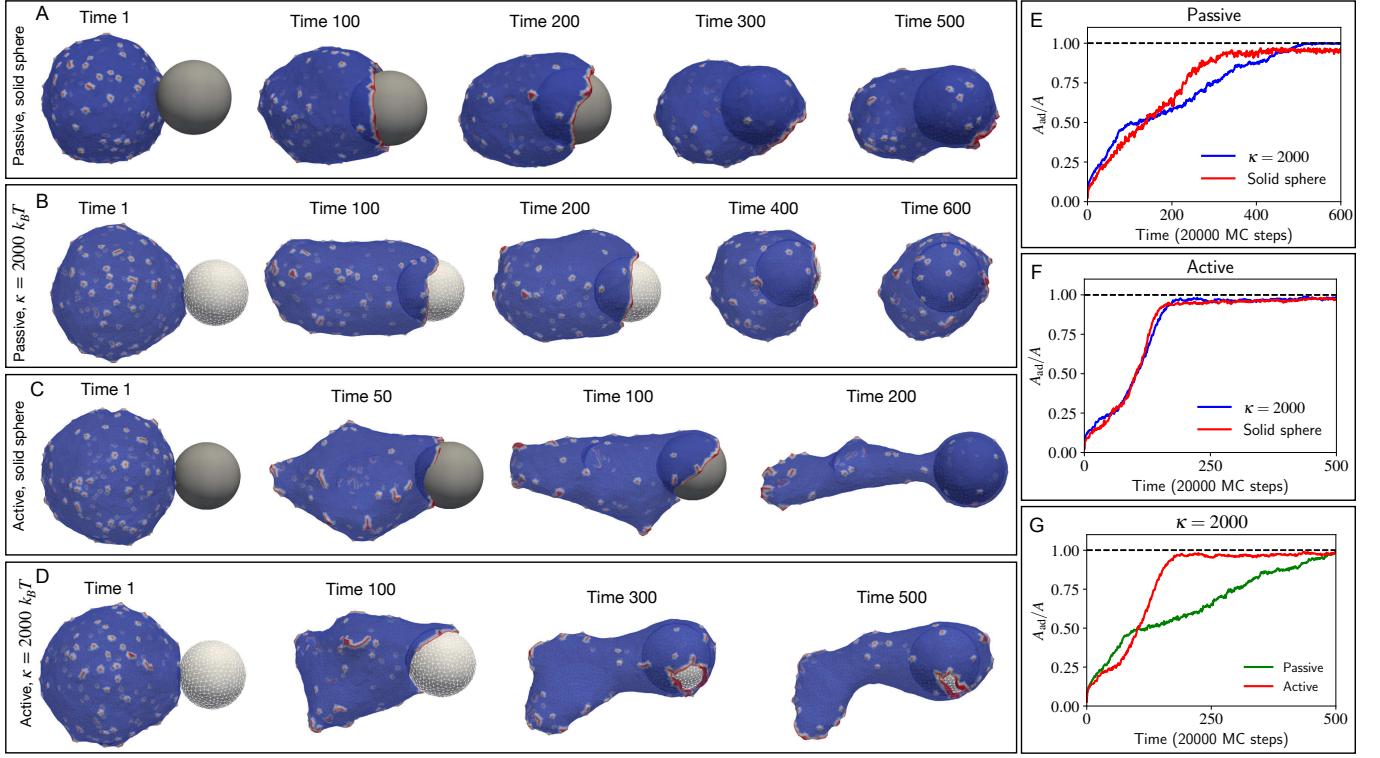


FIG. S6. The snapshots of the phagocytosis process when the big vesicle with passive proteins (no. of vertices  $N = 3127$ , no. of passive proteins  $N_p = 150$ , and bending rigidity  $\kappa = 20 k_B T$ ) tries to engulf a (A) rigid sphere of radius  $R = 10 l_{min}$  and (B) a vesicle (nearly a sphere of radius of  $R \approx 10 l_{min}$  in shape) with high bending rigidity  $\kappa^T = 2000 k_B T$ . Next, the big vesicle is active, it can exert force on the target. The active force parameter  $F = 2 k_B T l_{min}^{-2}$ . The snapshots are shown when the target is (C) a rigid sphere of radius  $R = 10 l_{min}$  and (D) a vesicle with high bending rigidity  $\kappa^T = 2000 k_B T$ . Comparison of the adhesive area fraction of the target between the rigid sphere and the vesicle of bending rigidity  $\kappa^T = 2000 k_B T$  when the engulfing vesicle is (E) passive  $F = 0$  and (F) active case  $F = 2 k_B T l_{min}^{-2}$ . (G) Comparison of the adhesive area fraction of the target between the passive and active engulfment.

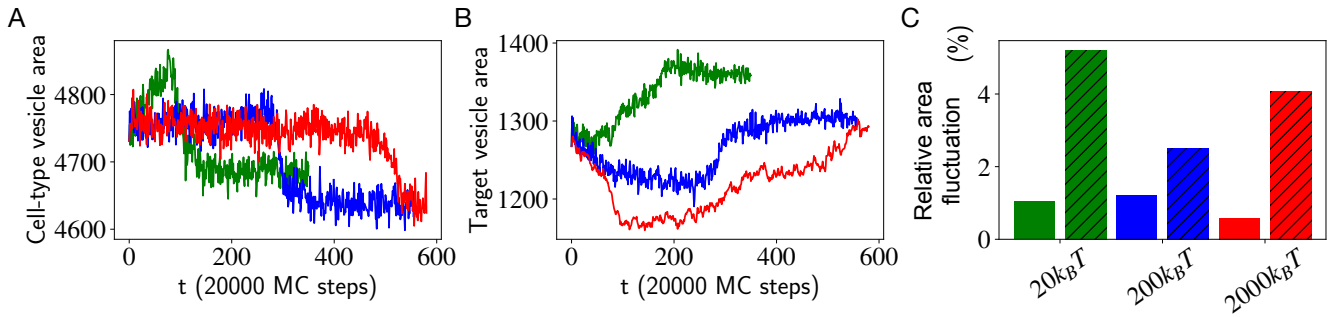


FIG. S7. The evolution of the vesicles' area during the engulfment simulations for the passive case (Fig.3): A) The cell-like vesicle area over time, for three different bending rigidity values of the target vesicle:  $\kappa = 20, 200, 2000$  respectively in the units  $k_B T$  (green, blue and red respectively). B) The target vesicle's area over time, as in (A). C) The relative fluctuation of the area for both vesicles is calculated with respect to the initial area of the vesicle. The smooth-color bars are for the cell-like vesicle, while the diagonal hatched bars are for the target vesicle.

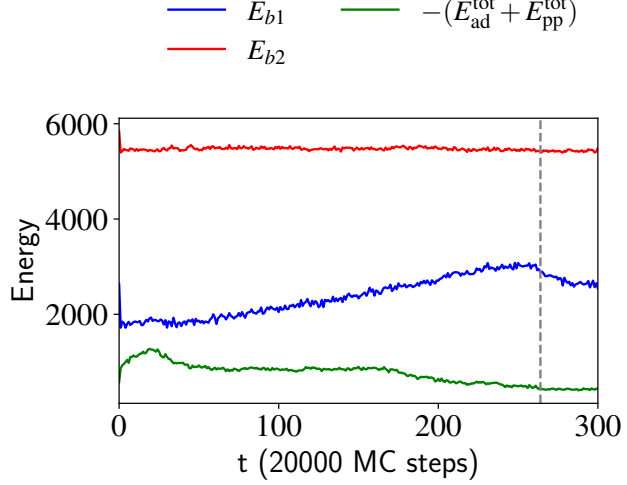


FIG. S8. The timeseries for the energy terms for the case of pushing (Fig.4D), when the bending rigidity of the target is  $\kappa = 200 k_B T$ . The bending energy of the target vesicle is nearly constant over time (red). We show the competition between the bending energy of the cell-like vesicle (blue) and its adhesion and protein-protein interaction energies (green). The grey dashed line indicates the time when the cell-like vesicle detached from the target vesicle. This detachment allows the cell-like vesicle to retract its long thin protrusion, thereby reducing its bending energy.

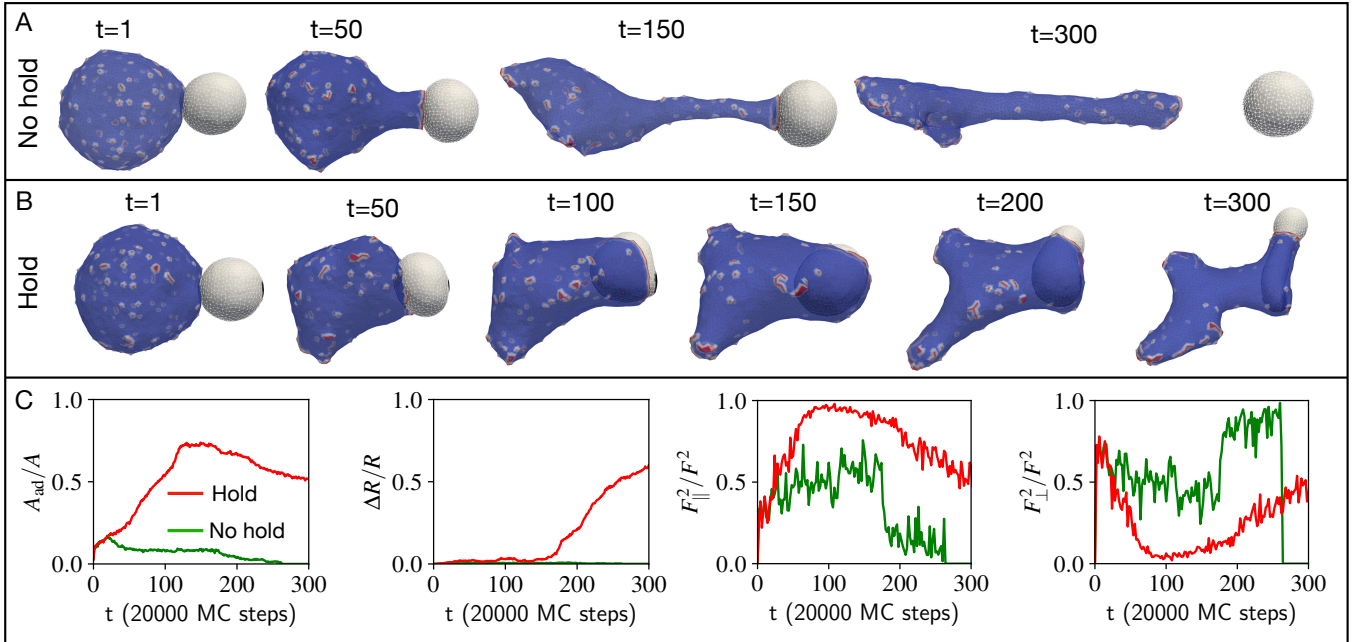


FIG. S9. Comparison of the dynamics in the pushing regime for free and confined target vesicle. A) Snapshots of the pushing event when the target is free here (as in Fig.4D,  $\kappa = 200 k_B T$ ). B) Snapshots of the same process when the target vesicle has a small patch of vertices which is fixed and not allowed to move. This patch is denoted by black color at the pole of the target vesicle opposite the cell-like vesicle at the initial time. C) Comparison of the time series for (A,B in green and red respectively) of the adhered area fraction, rounded-ness, tangential force fraction, and normal force fraction, respectively.

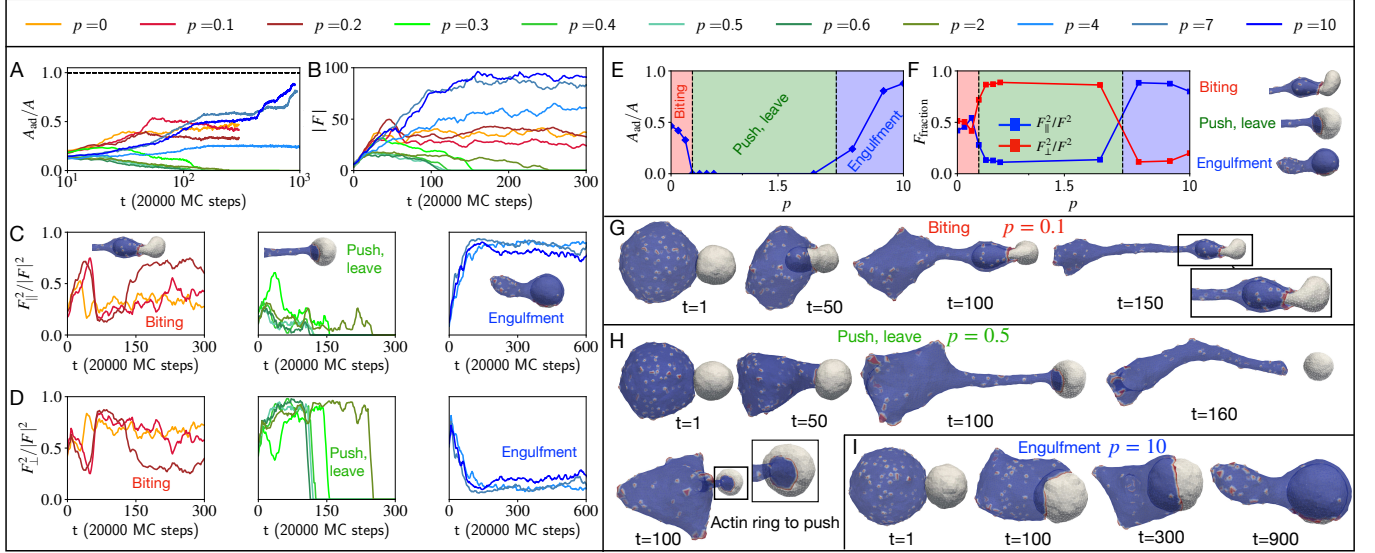


FIG. S10. Effect of the internal pressure of the target cell on the process of phagocytosis. The smaller vesicle (target) and the bigger vesicle (attacking cell) are made of 847 and 3127 vertices, respectively. The time evolution of the adhesive area fraction and magnitude of the force applied on the target cell by the attacking cell are shown in A) and B), respectively. C) It shows the fraction of tangential force on the target for three different cases of nibbling, push-leave, and engulfment in three different panels. D) Similarly, the fraction of normal or pushing force on the target for three different cases of nibbling, push-leave, and engulfment in three different panels. E) We have shown the steady state average value of adhesive area fraction with the bending rigidity  $\kappa$  of the target cell. F) Here, we averaged the tangential and normal force fraction in the relevant time windows. (G-I) The time evolution of the shapes and the snapshots are shown for three different cases of nibbling, push-leave, and engulfment respectively.

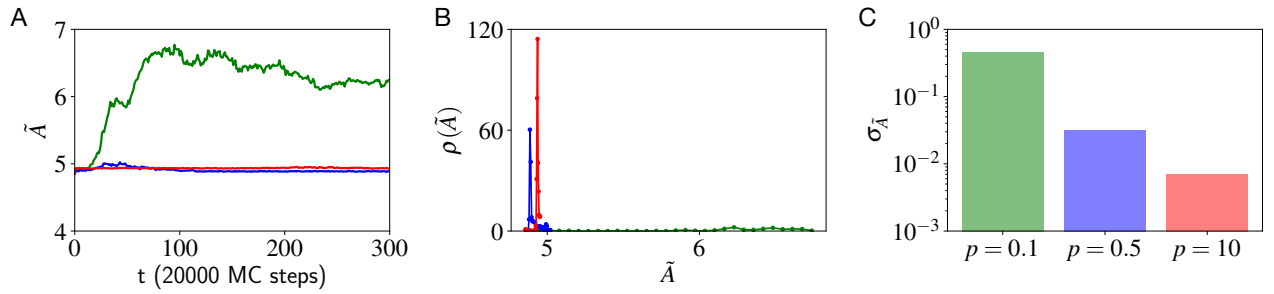


FIG. S11. A measure of membrane tension when the area and the volume both change over time during the active engulfment of a target-like vesicle with different internal pressure (Fig7G-I). A) The size normalised area  $\tilde{A}$  (Eq.S13) for three different pressure differences  $p = 0.1$ ,  $p = 0.5$ , and  $p = 10$  shown in green, blue and red, respectively. B) The probability distribution of the size normalized area  $\rho(\tilde{A})$ . C) The standard deviation  $\sigma_{\tilde{A}}$  of the size-normalized area. Higher tension results in lower standard deviation of the area fluctuations, and therefore higher internal pressure implies higher membrane tension. We set the bending rigidity of both the vesicles to  $2k_B T$ . The active force parameter  $F = 2k_B T$ , adhesion energy per node is  $E_{ad} = 2k_B T$  between the two vesicles.

---

- [1] C. E. Cornell, A. Chorlay, D. Krishnamurthy, N. R. Martin, L. Baldauf, and D. A. Fletcher. Target cell cortical tension regulates macrophage trogocytosis. *Nature Cell Biology*, pages 1–11, 2025.
- [2] T. Mareš, M. Daniel, A. Iglič, V. Kralj-Iglič, and M. Fošnarič. Determination of the strength of adhesion between lipid vesicles. *The Scientific World Journal*, 2012(1):146804, 2012.
- [3] R. K. Sadhu, S. R. Barger, S. Penič, A. Iglič, M. Krendel, N. C. Gauthier, and N. S. Gov. A theoretical model of efficient phagocytosis driven by curved membrane proteins and active cytoskeleton forces. *Soft Matter*, 19(1):31–43, 2023.
- [4] R. K. Sadhu, A. Iglič, and N. S. Gov. A minimal cell model for lamellipodia-based cellular dynamics and migration. *Journal of Cell Science*, 136(14):jcs260744, 2023.
- [5] R. K. Sadhu, S. Penič, A. Iglič, and N. S. Gov. Modelling cellular spreading and emergence of motility in the presence of curved membrane proteins and active cytoskeleton forces. *The European Physical Journal Plus*, 136(5):495, 2021.